

# O and Fe abundance correlations and distributions inferred for the thick and thin disk

R. Caimmi\*

November 14, 2021

## Abstract

A linear  $[\text{Fe}/\text{H}]-[\text{O}/\text{H}]$  relation is found for different stellar populations in the Galaxy (halo, thick disk, thin disk) from a data sample obtained in a recent investigation (Ramírez et al. 2013). These correlations support previous results inferred from poorer samples: stars display a “main sequence” expressed as  $[\text{Fe}/\text{H}] = a[\text{O}/\text{H}] + b \mp \Delta b$  where a unit slope,  $a = 1$ , implies a constant  $[\text{O}/\text{Fe}]$  abundance ratio. Oxygen and iron empirical abundance distributions are then determined for different subsamples, which are well explained by the theoretical predictions of multistage closed-(box+reservoir) (MCBR) chemical evolution models by taking into account the found correlations. The interpretation of these distributions in the framework of MCBR models gives us clues about inflow/outflow rates in these different Galactic regions and their corresponding evolution. Outflow rate for the thick and the thin disks are lower than the halo outflow rate. Moreover if the thin disk built up from the thick disk, both systems result of comparable masses. Besides that, the iron-to-oxygen yield ratio and the primary to not primary contribution ratio for the iron production are obtained from the data, resulting consistent with SNII progenitor nucleosynthesis and with the iron production from SNIa supernova events.

---

\**Physics and Astronomy Department, Padua Univ., Vicolo Osservatorio 3/2, I-35122 Padova, Italy* email: roberto.caimmi@unipd.it fax: 39-049-8278212

*keywords - Galaxy: evolution - Galaxy: formation - stars: evolution - stars: formation.*

# 1 Introduction

Simple models of chemical evolution rely on some basic assumptions, namely (1) universal stellar initial mass function (IMF), which implies identical star generations both in space and in time, regardless of composition; (2) instantaneous recycling, which implies short-lived stars instantaneously die and long-lived stars exist forever; (3) instantaneous mixing, which implies gas returned from dying stars and gas inflowing from outside are instantaneously and uniformly mixed with the pre-existing gas; (4) universal nucleosynthesis for assigned stellar mass, which implies nuclide production is independent of the initial composition. For further details and application to the solar neighbourhood, an interested reader is addressed to earlier investigations on disk (e.g., Pagel and Patchett 1975) and halo (e.g., Ryan and Norris 1991) stars.

In reality, the above mentioned assumptions are valid only to a first extent. More specifically, (1) leaving aside pop III stars, a top-heavy IMF seems to be triggered by tidal interactions due to merger or accretion events (e.g., Rieke et al. 1980; Doane and Mathews 1993; Lopez-Sanchez 2010) while, on the other hand, the IMF lower end depends on the temperature, pressure and composition of gas turned into a star generation (e.g., Conroy et al. 2013; Bekki 2013); (2) gas recycling after star death is delayed for long-lived stars such as type Ia supernova (SNIa) progenitors (e.g., Haywood 2001); (3) gas returned after star death or inflowing from outside is uniformly mixed with the interstellar medium after a finite time, or restricted into cells with little interaction with the surroundings (e.g., Wilmes and Köppen 1995; Wiersma et al. 2009); (4) stellar nucleosynthesis depends on the initial composition, in addition to the initial mass, for a class of nuclides called secondary elements, in contrast with primary elements for which the dependence on the initial composition may be neglected to a first extent (e.g., Pagel and Tautvaišienė 1995). In particular, it holds for oxygen and iron created in massive stars or SNII events (e.g., Yates et al. 2013). Stellar lifetime also depends on the initial metal abundance, but the trend changes only slightly and can be neglected to a first extent (e.g., Yates et al. 2013).

Accordingly, simple models of chemical evolution can be used as a zeroth order approximation and comparison with results from more refined models could be useful. Let nuclides produced under the validity of assumptions (1)-(4) above be defined as simple primary (sp) elements (Caimmi 2013a, hereafter quoted as C13a) and nuclides produced otherwise be defined as non simple primary (np) elements. Let processes yielding sp and np elements be defined as sp and np processes, respectively.

In this scenario, predictions may be compared with observations from a

selected star sample and discrepancies could provide valuable informations on the history of the parent population. In particular, predicted relative mass abundances maintain constant,  $Z_{Q_1}/Z_{Q_2} = \text{const}$ , or  $Z_Q/Z = \text{const}$ , where  $Q_1, Q_2, Q$ , are selected elements heavier than He, or metals, and  $Z = \sum Z_{Q_i}$  where all metals are included.

In terms of number abundances normalized to solar values, according to the standard spectroscopic notation<sup>1</sup>, the above relation translates into  $[Q_1/H] = [Q_2/H] + b_{Q_1}$ , where  $b_{Q_1}$  depends on  $Z_{Q_1}/Z_{Q_2}$  and its solar counterpart (e.g., C13a). That is a relation which can be inferred from sample stars where both  $[Q_1/H]$  and  $[Q_2/H]$  are known.

To this aim, oxygen appears as a natural choice of sp element. In fact, it is mainly synthesized within type II supernova (SNII) progenitors, which makes the above assumptions (1)-(4) hold to an acceptable extent. Accordingly,  $[Q/H] = [O/H] + b_Q$  provided Q is also sp element, which is a straight line of unit slope and intercept,  $b_Q$ , on the  $\{O[O/H][Q/H]\}$  plane. On the other hand, an empirical  $[Q/H]-[O/H]$  relation may be obtained for any element (sp or np), when the number of objects is high enough, and then compared with theoretical predictions to determine the contribution of sp and np processes to the mass abundance,  $Z_{Q_{sp}}$  and  $Z_{Q_{np}}$ .

Classical simple models are closed-box (CB), allowing neither gas inflow nor gas outflow, which implies total (gas+star) mass remains unchanged (e.g., Pagel and Patchett 1975). The addition of a reservoir to the box opens the possibility of both gas inflow (from the reservoir to the box) and gas outflow (from the box to the reservoir), while the total mass remains unchanged provided the reservoir is included in the balance. In other words, the model may be conceived as “closed” with regard to the box+reservoir and “open” with regard to the box alone, or shortly closed-(box+reservoir) (CBR). For further details, an interested reader is addressed to the parent papers (Caimmi 2011a, 2012a). The first example of CBR model is shown in a classical paper where the predicted chemical evolution of the halo fits to the data (Hartwick 1976). Though the box and the reservoir are not explicitly mentioned therein, gas inhibited from star formation may safely be conceived as outflowing from the box (the halo therein) to the reservoir (the disk therein).

In general, CBR models maintain the standard assumptions mentioned above for CB models, with the addition of (i) mass conservation within the box+reservoir; (ii) gas outflow from the box into the reservoir or gas inflow into the box from the reservoir (1) at a rate proportional to the star formation

---

<sup>1</sup>In general,  $[Q_1/Q_2] = \log(N_{Q_1}/N_{Q_2}) - \log(N_{Q_1}/N_{Q_2})_{\odot}$ , where  $N_Q$  is the number density of the element, Q.

rate, and (2) with composition proportional to its counterpart within the box; (iii) absence of star formation within the reservoir.

Mass conservation within the box+reservoir can be expressed as (e.g., Caimmi 2011a):

$$(1 + \kappa) \frac{ds}{dt} = - \frac{d\mu}{dt} ; \quad (1)$$

where  $\kappa$  is the flow parameter (ratio of inflowing or outflowing gas rate to locking up gas rate into long-lived stars and remnants),  $s$  and  $\mu$  are long-lived star and gas mass fraction. More specifically, with respect to CB models, Eq. (1) discloses different flow regimes as: outflow regime ( $\kappa > 0$ ), where less gas is available for star formation (Hartwick 1976); stagnation regime ( $\kappa = 0$ ), where CBR models reduce to CB models (Searle 1972; Searle and Sargent 1972); moderate inflow regime ( $-1 < \kappa < 0$ ), where a slightly larger amount of gas is available for star formation and the gas mass fraction monotonically decreases in time (Caimmi 2007); steady inflow regime ( $\kappa = -1$ ), where a larger amount of gas is available for star formation and the gas mass fraction remains unchanged in time (Caimmi 2011a, 2012a); strong inflow regime ( $\kappa < -1$ ) where a substantially larger amount of gas is available for star formation and the gas mass fraction monotonically increases in time (Caimmi, 2011a, 2012a).

A main feature of CBR (and *a fortiori* CB) models is that the theoretical differential abundance distribution (TDAD),  $\psi_Q = \log[dN/(N d\phi_Q)]$ , as a function of the normalized abundance,  $\phi_Q = Z_Q/(Z_Q)_\odot$ , is close to a straight line for the cases of interest,  $\psi_Q = \alpha_Q \phi_Q + \beta_Q$ , where Q is a selected primary element synthesised within SNII progenitors and  $N$  the total number of long-lived stars (Pagel 1989; Malinie et al. 1993; Rocha-Pinto and Maciel 1996; Caimmi 2011a, 2012a, and earlier references therein). The normalized abundance, in turn, may be expressed to an acceptable extent as (e.g., Pagel and Patchett 1975; Hartwick 1979):

$$\phi_Q = - \frac{1}{1 + \kappa} \frac{\hat{p}_Q}{(Z_Q)_\odot} \ln \mu ; \quad (2)$$

where  $\hat{p}_Q/(1 + \kappa)$  is the effective yield. Accordingly, a linear (or nearly linear) fit to the empirical differential abundance distribution (EDAD) allows comparison between observations from stellar populations and predictions of CBR models. More specifically, oxygen EDAD can be fitted by a broken line with several segments, where each segment can be interpreted within the framework of CBR models. A change in the slope implies a transition between adjacent evolutionary stages.

In other words, oxygen EDAD can be reproduced via a chain of CBR models where the flow rate is discontinuous in each transition, or shortly mul-

tistage closed-(box+reservoir) (MCBR) models. In particular, early stages appear to undergo strong inflow regime, middle stages approach steady inflow regime, and late stages exhibit low inflow or outflow regime (Caimmi 2011a, 2012a). The special case of steady inflow regime, where the inflowing gas balances the amount of pre-existing gas turned into stars, finds a counterpart in the results of hydrodynamical simulations, where quasi equilibrium is attained between inflowing gas, outflowing gas, gas turned into stars (e.g., Finlator and Davé 2008; Davé et al. 2011a,b, 2012).

The main features of MCBR models (Caimmi 2011a, 2012a, 2013b, the last quoted henceforth as C13b), for any assigned sp element, Q, may be summarized as follows.

- Simple MCBR models predict a linear TDAD,  $\psi_Q = \alpha_Q \phi_Q + \beta_Q$ .
- The slope,  $\alpha_Q$ , and the intercept,  $\beta_Q$ , of this TDAD depend on the effective yield,  $\hat{p}_Q/(1 + \kappa)$ , on the initial abundance,  $(\phi_Q)_i$ , and on the initial and final gas mass fraction,  $\mu_i$  and  $\mu_f$ .
- The TDAD slope relates to the flow regime as follows. The steady state inflow regime ( $\kappa = -1$ ) implies null slope ( $\alpha = 0$ ). The strong inflow regime ( $\kappa < -1$ ) implies positive slope ( $\alpha > 0$ ). The weak inflow regime ( $-1 < \kappa < 0$ ), the stagnation regime ( $\kappa = 0$ ), and the outflow regime ( $\kappa > 0$ ) imply negative slope ( $\alpha < 0$ ).
- The abundance ratio between two sp elements remains fixed during the evolution and equals the yield ratio which, in turn, is inversely proportional to the TDAD slope ratio,  $\hat{p}_{Q_1}/\hat{p}_{Q_2} = [(Z_{Q_1})_{\odot}/(Z_{Q_2})_{\odot}](\alpha_{Q_2}/\alpha_{Q_1})$ .
- For two different populations, P<sub>1</sub>, P<sub>2</sub>, the TDAD slope ratio relates to the flow regime, as  $(\alpha_Q)_{P_1}/(\alpha_Q)_{P_2} = (1 + \kappa_{P_1})/(1 + \kappa_{P_2})$ .
- Any choice of input parameters (initial gas mass fraction,  $\mu_i$ ; initial star mass fraction,  $s_i$ ; initial inflowed/outflowed gas mass fraction,  $D_i$ ; initial and final element abundance normalized to the solar value,  $(\phi_Q)_i$ ,  $(\phi_Q)_f$ ; TDAD slope and intercept,  $\alpha_Q$ ,  $\beta_Q$ ; IMF,  $\Phi(m)$ ; true yield,  $\hat{p}_Q$ ) produce the output parameters (flow parameter,  $\kappa$ ; final gas mass fraction,  $\mu_f$ ; final star mass fraction,  $s_f$ ; final inflowed/outflowed gas mass fraction,  $D_f$ ) which can be taken as input parameters for the subsequent stage of evolution.

To this respect, MCBR models make a further step with respect to standard simple models, where a single stage is considered, in that a sequence of evolutionary stages is described, where the inflow/outflow rate and related

parameters change passing from a previous stage to a subsequent one. In this context, the predicted TDAD must necessarily relate to sp elements, oxygen in particular.

On the other hand, the EDAD is usually inferred from iron, which is easier to be detected in stellar atmospheres. But iron cannot be considered as instantaneously recycled (i.e. sp element) in that a substantial fraction is produced via SNIa events, whose progenitors are low-mass stars ( $m \lesssim 8m_{\odot}$ ) belonging to binary systems where the members are sufficiently close.

Then in absence of oxygen abundance data inferred from observations, an empirical  $[\text{Fe}/\text{H}]-[\text{O}/\text{H}]$  relation (e.g., Carretta et al. 2000; Israelian et al. 2001) has necessarily to be used for determining oxygen EDAD from a selected star sample.

In earlier papers, a linear fit to the empirical  $[\text{Fe}/\text{H}]-[\text{O}/\text{H}]$  relation has been aimed to different extents: (a) to infer oxygen EDAD from iron EDAD in absence of rich samples where oxygen abundance is known, such as halo stars (Caimmi 2011a); (b) to provide a rigorous star classification within globular clusters and other halo and disk populations (C13a). An additional result, restricted to iron fraction synthesised within SNII progenitors, is that the iron-to-oxygen yield ratio can be independently expressed via either a linear  $[\text{Fe}/\text{H}]-[\text{O}/\text{H}]$  relation with a unit slope regardless of iron and oxygen TDAD, or a linear iron and oxygen TDAD regardless of  $[\text{Fe}/\text{H}]-[\text{O}/\text{H}]$  relation (C13b).

According to the above considerations, with regard to a selected element, Q, and to an assigned star sample, both the inferred empirical  $[\text{Q}/\text{H}]-[\text{O}/\text{H}]$  relation and the EDAD for Q and O provide valuable clues for understanding the evolution of the parent population. In most cases,  $\text{Q} = \text{Fe}$ , as iron can easily be detected.

The current paper deals with a sample including halo, thick disk and thin disk nearby stars, for which both oxygen and iron abundances have been well determined (Ramírez et al. 2013, hereafter quoted as Ra13) as extension of a previous investigation (Ramírez et al. 2007). More specifically, rich sub-samples are available with accurate abundance values for disk populations, with the addition of a poor incomplete halo sample (Ramírez et al. 2012).

By using this much better sample of stars with available data for oxygen and iron, we would like to check our previous finding and conclusions doing what follows:

- (i) completely studying O-Fe correlations,
- (ii) determining oxygen and iron EDAD,

- (iii) performing linear fits to oxygen and iron EDAD above and comparing with related TDAD in the framework of MCBR models,
- (iv) checking that the iron EDAD obtained from oxygen EDAD and  $[\text{Fe}/\text{H}]$ - $[\text{O}/\text{H}]$  relation reproduces the actually measured iron EDAD,
- (v) determining sp and np iron contributions from  $[\text{Fe}/\text{H}]$ - $[\text{O}/\text{H}]$  relation,
- (vi) estimating the ratio between yields for iron and oxygen,
- (vii) analysing the above results in the framework of MCBR models to estimate the outflow and inflow rates.
- (viii) obtaining the thick disk evolution and comparing these results with other conclusions inferred from age and star formation rates (Haywood et al. 2013; Snaith et al. 2014).

Basic informations on the data together with regression line analysis are provided in Section 2, where the original sample is subsampled according to star population and star class. The inferred EDAD for oxygen and iron are shown in Section 3. The results are discussed in Section 4. The conclusion is drawn in Section 5.

## 2 Data and regression line analysis

The data are taken from a sample ( $N = 825$ ) of solar neighbourhood FGK-type dwarf stars in the metallicity range,  $-2.6 < [\text{Fe}/\text{H}] < 0.5$ , for which  $[\text{O}/\text{H}]$  has been determined using high-quality spectra and a non-LTE analysis of the 777 nm OI triplet lines, while a standard spectroscopic approach has been followed for the evaluation of  $[\text{Fe}/\text{H}]$ , where values of FeII have been taken as representative. For further details, an interested reader is addressed to Ra13 and earlier researches (Ramírez et al. 2007, 2012).

Subsamples can be extracted from the parent sample (HD) according to different populations and different classes: a star of the sample belongs to halo (HH), thick disk (KD), or thin disk (ND), if  $P_{XY} > 0.5$ , where  $XY = \text{HH}, \text{KD}, \text{ND}$ , and  $P$  is a probability inferred from kinematics, or it is uncertain between thick and thin disk (KN), when  $P_{\text{KD}} \leq 0.5$ ,  $P_{\text{ND}} \leq 0.5$ ,  $P_{\text{HH}} \ll \min(P_{\text{KD}}, P_{\text{ND}})$ , respectively. It is worth noticing the above mentioned uncertainty criterion, which prevents a disk star from being assigned to the thick or thin subsystem, is more restrictive with respect to what assumed in Ra13.

Table 1: Number of stars in the subsamples from the original sample for different populations (pop) as: ND - thin disk; KD - thick disk; KN - uncertain if belonging to thin or thick disk; HH - halo; HD - original sample (HD = ND + KD + KN + HH); and class (cl) as: n - normal dwarfs; c - cool high-metallicity dwarfs; g - giants; o - outliers; t - total (t = n + c + g + o).

pop: cl	ND	KD	KN	HH	HD
n	513	215	6	41	775
c	10	1	0	0	11
g	14	18	0	3	35
o	1	3	0	0	4
t	538	237	6	44	825

According to Ra13, sample stars are classified as cool high-metallicity dwarfs ( $T_{\text{eff}} < 5100 \text{ K}$ ;  $\log g > 4.4$ ;  $[\text{Fe}/\text{H}] > -0.1$ ), giants ( $T_{\text{eff}} < 5500 \text{ K}$ ;  $\log g < 4.0$ ), outliers (relative to the main disk  $[\text{O}/\text{Fe}]$  vs.  $[\text{Fe}/\text{H}]$  trend), which shall be denoted throughout the text as c, g, o, respectively. The remaining stars are classified here as “normal” dwarfs and denoted as n.

The number of stars belonging to different subsamples, as given in Ra13, are listed in Table 1. Subsamples related to a stellar population and a selected class shall be denoted as XYZ, where XY defines the population, as shown below with the addition of XY = KN, HD, and z defines the star class, z = n, c, g, o. Though halo subsamples are largely incomplete, still they shall be considered for inference of preliminary results and comparison with related disk counterparts.

The empirical  $[\text{Fe}/\text{H}]$ - $[\text{O}/\text{H}]$  relation is plotted in Fig. 1 for the parent sample, HD, where different star classes are denoted by different symbols, as squares (NDn), saltires (KDn), diagonalized squares (KNn), crosses (HHn), triangles (HDc), diamonds (HDg), “at” (HDo).

Also shown are three selected “main sequences”, expressed as:

$$[\text{Fe}/\text{H}] = [\text{O}/\text{H}] - 0.45 \mp 0.25 \quad ; \quad (3)$$

(dotted), already shown in earlier researches (Caimmi 2012a; C13a);

$$2[\text{Fe}/\text{H}] = 3[\text{O}/\text{H}] - 0.25 \mp 0.75 \quad ; \quad (4)$$

(dashed), inferred from Ra13;

$$3[\text{Fe}/\text{H}] = 4[\text{O}/\text{H}] - 0.40 \mp 0.80 \quad ; \quad (5)$$

Table 2: HIP number, oxygen and iron abundance, related uncertainty ( $\Delta_Q = \Delta[Q/H]$ ,  $Q = O, Fe$ ), population and class (XYZ), for stars lying outside (including the errors) the main sequences with slope equal to  $4/3$  and  $3/2$ , respectively, plotted in Fig. 1. For further details refer to the text.

HIP	[O/H]	$\Delta_O$	[Fe/H]	$\Delta_{Fe}$	XYZ
069972	+0.55	0.12	+0.16	0.13	NDc
060719	-0.78	0.32	-2.44	0.13	KDg
049988	-0.53	0.26	-0.81	0.05	KDo
012294	-0.88	0.01	-0.77	0.22	HHn
068594	-3.83	1.48	-2.56	0.06	HHg
114962	-1.15	0.02	-1.24	0.23	HHn

(full), inferred from Fig. 1.

Keeping in mind typical errors are of the order of symbol dimensions on the scale of the plot, an inspection of Fig. 1 shows a substantial fraction of sample stars lie outside the main sequence of slope equal to 1. Accordingly, iron cannot be considered as a simple primary element, contrary to oxygen, mainly due to delayed recycling via SNIa events.

On the other hand, only a few stars lie outside the main sequences with slope equal to  $4/3$  and  $3/2$ , respectively, whose abundances and related uncertainties are listed in Table 2. It includes stars from different populations and classes: NDc (1), KDg (1), KDo (1), HHn (2), HHg (1), for a total of 6. In this view, the stars under discussion should be considered as outliers.

In addition, the HHg star lies outside the scale of related plots and cannot be represented even in the parent paper (Ra13). If inferred oxygen abundance is unbiased, the above mentioned star could be a globular cluster outlier of second or later generation, which implies sodium overabundance (Ramírez et al. 2012).

The empirical [Fe/H]-[O/H] relation is plotted in Fig. 2 for ND, KD, HH subsamples and the parent sample, HD, the last repeated for better comparison. Within the current framework, all stars belonging to HH, KD, ND, DD = KD + ND + KN subsamples could be used to infer both the [Fe/H]-[O/H] empirical relation and the EDAD for O and Fe. On the other hand, the empirical [O/Fe]-[Fe/H] relation is inferred in Ra13 using stars of class n only, which are the main part of sample stars as shown in Table 1. Accordingly, to be consistent with the results of Ra13, further analysis shall be restricted to stars of class n and, to save space, subsamples HHn, KDn, NDn, DDn, HDn, shall hereafter be denoted as HH, KD, ND, DD, HD, respectively.

Table 3: Regression line slope and intercept estimators,  $\hat{a}$  and  $\hat{b}$ , and related dispersion estimators,  $\hat{\sigma}_{\hat{a}}$ , and  $\hat{\sigma}_{\hat{b}}$ , for different subsamples (sub) . The number ( $N$ ) of stars within each subsample is also listed.

$\hat{a}$	$\hat{\sigma}_{\hat{a}}$	$-\hat{b}$	$\hat{\sigma}_{\hat{b}}$	sub	$N$
1.1743D+00	4.7182D-02	2.2727D-01	3.6619D-02	HH	041
1.6015D+00	4.4402D-02	1.6873D-01	9.0781D-03	KD	215
1.3658D+00	2.9746D-02	7.0718D-02	5.1026D-03	ND	513
1.5942D+00	4.8154D-02	9.5685D-02	7.8672D-03	DD	734
1.4378D+00	5.0321D-02	1.0174D-01	7.9502D-03	HD	775

At this stage, two considerations can be performed. First, the sample consists of nearby stars, which implies that our conclusions rely on the assumption that the solar neighbourhood is a typical region of the related subsystem (ND, KD, HH). Second, although a bilinear regression with a knee has been widely used for fitting the [O/Fe]-[Fe/H] empirical relation (e.g., Ra13), we prefer a single linear regression. The dichotomy between bilinear (e.g., Carretta et al. 2000; Gratton et al. 2000) and linear (e.g., Israelian et al. 2001; Takada-Hidei et al. 2001) trend is long-dating, but the last alternative is preferred here, as in previous works (Caimmi 2012a; C13a), for reasons of simplicity.

In summary, number abundances plotted in Fig. 2 show a linear trend as:  $[\text{Fe}/\text{H}] = a[\text{O}/\text{H}] + b$  for HH, KD, ND, DD, HD populations. The regression line has been determined for each subsample using standard methods (e.g., Isobe et al. 1990; Caimmi 2011b, 2012b) and the results are listed in Table 3 and plotted in Fig. 3. From these results, it is evident that:

- (1) The regression line slope estimators,  $\hat{a}$ , are not consistent<sup>2</sup> within  $\mp 3\hat{\sigma}_{\hat{a}}$ , for HH, KD, ND populations and the same holds for DD, HD populations.
- (2) The regression line slope estimators are not consistent with the unit slope, within  $\mp 3\hat{\sigma}_{\hat{a}}$ , regardless of the population.
- (3) The regression line intercept estimators,  $\hat{b}$ , are not consistent within

<sup>2</sup> The term ‘‘consistent’’ has to be intended in mathematical (instead of statistical) sense, as a null intersection between intervals,  $\hat{x} \mp \hat{\sigma}_{\hat{x}}$ , related to different populations, where  $x$  is a random variable.

$\mp 3\hat{\sigma}_i$  for HH, KD, ND populations and the same holds for DD, HD populations.

These different slope and intercept values for different populations imply a different chemical evolution for each region (HH, KD, ND, or DD if KD and ND evolve as a single system).

### 3 Results

The EDAD,  $\psi_Q = \log[\Delta N/(N\Delta\phi_Q)]$ , inferred from HH, KD, ND, DD subsamples, is listed in Tables 4-5 for oxygen and iron ( $Q = \text{O}, \text{Fe}$ ), respectively. Data are equally binned in  $[\text{Q}/\text{H}]$  taking  $\Delta[\text{Q}/\text{H}] = \Delta \log \phi_Q = 1\text{dex}$ , where the normalized abundance,  $\phi_Q$ , is listed in the first column, while the EDAD,  $\psi_Q$ , and the number,  $\Delta N$ , of subsample stars within the abundance range,  $\exp_{10}(\log \phi_Q \mp \Delta \log \phi_Q)$ , are listed in the following columns for each related stellar population. Uncertainties in  $\psi_Q$ ,  $\Delta^\mp \psi_Q$ , are calculated as Poissonian errors, which implies  $\Delta^- \psi_Q \rightarrow \infty$  for bins populated by a single star,  $\Delta N = 1$ .

The above mentioned EDAD is plotted in Figs. 4-5 for O and Fe, respectively, separating results for each stellar population (ND, KD, DD = ND + KD + KN, and HH) in a different panel. Lower uncertainties attaining the horizontal axis (decreasing down to negative infinity) relate to bins populated by a single star. Regression lines (dashed lines) have been performed to points in each stage (defining bins populated by at least two stars).

Arithmetic mean and rms error can be inferred from the EDAD as (C13a; C13b):

$$\overline{\log \phi} = \overline{[\text{Q}/\text{H}]} = \frac{1}{N} \sum_{i=1}^N [\text{Q}/\text{H}]_i \quad ; \quad (6)$$

$$\sigma_{\log \phi} = \sigma_{[\text{Q}/\text{H}]} = \left\{ \frac{1}{N-1} \sum_{i=1}^N \left( [\text{Q}/\text{H}]_i - \overline{[\text{Q}/\text{H}]} \right)^2 \right\}^{1/2} \quad ; \quad (7)$$

where  $Q = \text{O}, \text{Fe}$ , and  $N$  is the subsample population. The results are listed in Table 6 for subsamples, HH, KD, ND, DD.

### 4 Discussion

The following main points shall be discussed throughout the current section, concerning (1) abundance distributions and their interpretation within the framework of simple MCBR models, where special effort is devoted to inflow

Table 4: Oxygen empirical differential abundance distribution (EDAD), inferred from different subsamples, where  $\delta = \Delta N$  to save space. See text for further details.

subsample:	HH		KD		ND		DD	
$\phi_{\text{O}}$	$\psi_{\text{O}}$	$\delta$	$\psi_{\text{O}}$	$\delta$	$\psi_{\text{O}}$	$\delta$	$\psi_{\text{O}}$	$\delta$
2.5286D-2	+9.2507D-1	2						
3.1833D-2	+1.0012D+0	3						
4.0075D-2								
5.0451D-2	+3.2404D-1	1						
6.3514D-2	+2.2404D-1	1						
7.9960D-2	+1.2404D-1	1						
1.0066D-1	+5.0116D-1	3						
1.2673D-1	+2.2507D-1	2						
1.5954D-1	-1.7596D-1	1	-8.9561D-1	1			-1.4289D+0	1
2.0085D-1	+3.2610D-1	4	-5.1849D-1	3			-1.0518D+0	3
2.5286D-1	+5.2713D-1	8	-7.9458D-1	2			-1.3278D+0	2
3.1833D-1	-1.7493D-1	2	-4.1746D-1	6	-8.7432D-1	5	-6.8748D-1	11
4.0075D-1	+1.2301D-1	5	-2.1643D-1	12	-6.7329D-1	10	-4.8645D-1	22
5.0451D-1	+3.7493D-1	2	+3.5751D-2	27	-1.2984D-1	44	-7.7612D-2	71
6.3514D-1	-2.9884D-1	3	+6.0689D-2	36	+7.5216D-3	76	+2.4208D-2	113
7.9960D-1	-5.7493D-1	2	+9.4583D-2	49	-9.5042D-3	92	+2.3418D-2	142
1.0066D+0	-9.7596D-1	1	-9.3553D-2	40	+7.2836D-2	140	+3.1201D-2	182
1.2673D+0			-3.9767D-1	25	-1.5626D-1	104	-2.1828D-1	129
1.5954D+0			-9.9252D-1	8	-7.2922D-1	35	-7.8542D-1	44
2.0085D+0			-1.2175D+0	6	-1.6743D+0	5	-1.4497D+0	12
2.5286D+0					-2.1723D+0	2	-2.3278D+0	2
total:		41		215		513		734

Table 5: Iron empirical differential abundance distribution (EDAD), inferred from different subsamples, where  $\delta = \Delta N$  to save space. See text for further details.

subsample:	HH		KD		ND		DD	
$\phi_{\text{Fe}}$	$\psi_{\text{Fe}}$	$\delta$	$\psi_{\text{Fe}}$	$\delta$	$\psi_{\text{Fe}}$	$\delta$	$\psi_{\text{Fe}}$	$\delta$
5.0451D-3	+1.6251D+0	2						
6.3514D-3								
7.9960D-3								
1.0066D-2	+1.0240D+0	1						
1.2673D-2	+1.2251D+0	2						
1.5954D-2	+8.2404D-1	1						
2.0085D-2								
2.5286D-2								
3.1833D-2	+8.2507D-1	2						
4.0075D-2								
5.0451D-2	+3.2404D-1	1						
6.3514D-2	+7.0116D-1	3	-1.9458D-1	2			-7.2784D-1	2
7.9960D-2	+4.2507D-1	2	-2.9458D-1	2			-8.2784D-1	2
1.0066D-1	+7.2301D-1	5	-6.9561D-1	1			-1.2289D+0	1
1.2673D-1	+7.0219D-1	6	-3.1849D-1	3			-8.5175D-1	3
1.5954D-1	+6.6914D-1	7	+3.3484D-1	17	-9.7226D-1	2	-1.5012D-1	19
2.0085D-1	+2.5071D-2	2	+2.5966D-1	18	-7.7123D-1	4	-1.8645D-1	22
2.5286D-1			+1.0851D-1	16	-3.5935D-1	13	-1.6647D-1	29
3.1833D-1	+2.2301D-1	5	+2.5154D-1	28	-2.9454D-1	19	-5.6773D-2	47
4.0075D-1	-5.7596D-1	1	+1.1936D-1	26	+1.2605D-1	63	+1.2052D-1	89
5.0451D-1			-1.5402D-2	24	+5.2783D-2	67	+3.0171D-2	91
6.3514D-1	-7.7596D-1	1	-1.5319D-1	22	-5.3748D-2	66	-8.4388D-2	88
7.9960D-1			-2.9458D-1	20	-7.0202D-2	80	-1.2887D-1	100
1.0066D+0			-6.5422D-1	11	-4.7986D-2	106	-1.6068D-1	117
1.2673D+0			-7.5422D-1	11	-4.2510D-1	56	-5.0280D-1	67
1.5954D+0			-1.0505D-0	7	-8.2613D-1	28	-8.8480D-1	35
2.0085D+0			-1.2966D-0	5	-1.6743D+0	5	-1.5289D+0	10
2.5286D+0			-1.7946D-0	2	-1.8712D+0	4	-1.8507D+0	6
total:		41		215		513		734

Table 6: Star number,  $N$ , mean abundance,  $\overline{[Q/H]}$ , rms error,  $\sigma_{[Q/H]}$ ,  $Q = O, Fe$ , inferred for different subsamples (sub). See text for further details.

$N$	$\overline{[O/H]}$	$\sigma_{[O/H]}$	$\overline{[Fe/H]}$	$\sigma_{[Fe/H]}$	sub
41	-0.6915	0.4274	-1.0393	0.5020	HH
215	-0.1172	0.1979	-0.3564	0.3174	KD
513	-0.0511	0.1580	-0.1401	0.2161	ND
734	-0.0699	0.1733	-0.2028	0.2690	DD

and outflow considerations, and evolution of different regions; (2) iron yields related to both sp and np processes, and oxygen-to-iron yield ratios.

## 4.1 Abundance distributions and their interpretation

### 4.1.1 Oxygen and iron TDAD

The theoretical differential abundance distribution (TDAD),  $\psi_Q = \log[dN/(N d\phi_Q)]$ , predicted by simple MCBR chemical evolution models, is a broken line (e.g., Caimmi 2011a, 2012a). The straight line defined by each segment can be expressed as (Pagel 1989):

$$\psi_Q = \alpha_Q \phi_Q + \beta_Q ; \quad (8)$$

$$\phi_Q = \frac{Z_Q}{(Z_Q)_\odot} ; \quad \phi_H = \frac{X}{X_\odot} ; \quad (9)$$

where  $X = Z_H$  according to the standard notation,  $Q$  is a selected element heavier than He (O and Fe in our case),  $\log \phi_Q = [Q/H]$  as a good approximation and  $(Z_Q)_\odot$  is the solar abundance.

The explicit expression of TDAD slope and intercept reads (e.g., Caimmi 2011a, 2012a):

$$\alpha_Q = -\frac{1}{\ln 10} \frac{(Z_Q)_\odot}{\hat{p}_Q} (1 + \kappa) ; \quad (10)$$

$$\beta_Q = \log \left[ \frac{\mu_i}{\mu_i - \mu_f} (-\ln 10) \alpha_Q \right] - \alpha_Q (\phi_Q)_i ; \quad (11)$$

where  $\hat{p}_Q$  is the yield per stellar generation (e.g., Pagel and Patchett 1975) of the sp element,  $Q$ , and  $\kappa$  is the flow parameter,  $\mu$  the active (i.e. available for star formation) gas mass fraction, i and f denote values at the start (minimum

Q abundance) and the end (maximum Q abundance) of the stage considered, respectively.

More specifically, the following flow regimes can be defined (e.g., Caimmi 2011a, 2012a): outflow ( $\kappa > 0$ ), where star formation is lowered (Hartwick 1976); stagnation ( $\kappa = 0$ ), where star formation is neither lowered nor enhanced; weak inflow ( $-1 < \kappa < 0$ ), where star formation is weakly enhanced and gas mass fraction monotonically decreases in time (Caimmi 2007); steady inflow ( $\kappa = -1$ ), where star formation is moderately enhanced and gas mass fraction remains unchanged; strong inflow ( $\kappa < -1$ ), where star formation is strongly enhanced and gas mass fraction monotonically increases in time.

Owing to Eq. (10), strong inflow, steady inflow, weak inflow or stagnation or outflow, imply positive, null, negative TDAD slope, respectively. In current  $\Lambda$ CDM scenarios, strong inflow may safely be related to an assembling stage of galaxy evolution, steady state inflow to a formation stage, weak inflow or stagnation or outflow to a next evolution stage (e.g., Finlator and Davé 2008; Davé et al. 2011a,b, 2012).

#### 4.1.2 Oxygen and iron EDAD

Within the framework of simple MCBR chemical evolution models, the TDAD of sp elements may be considered in connection with different stages of evolution. More specifically, the early stage with positive slope relates to strong gas inflow (SI), where the gas mass fraction is increasing in time; the middle stage with nearly flat slope relates to (nearly) steady state gas inflow (SS), where the gas mass fraction remains (more or less) unchanged in time; the late stage with negative slope relates to weak gas inflow or outflow (WI), where the gas mass fraction is decreasing in time.

Oxygen and iron EDAD shown in Fig. 4 and 5, respectively, for disk populations is characterized by three distinct stages exhibiting different linear trends. For each stage, regression lines shown in Figs. 4-5 have been determined using standard methods (e.g., Isobe et al. 1990; Caimmi 2011b, 2012b), leaving aside points related to bins containing a single star, where  $\Delta^- \psi_Q \rightarrow \infty$ . The regression procedure has been performed on HH, KD, ND, DD subsamples and the results are shown in Tables 7-8 for oxygen and iron, respectively. The transition points between adjacent stages are determined as intersections of related regression lines and the results are shown in Table 9 for both oxygen and iron, which are marked as dotted vertical lines in Figs. 4 and 5, respectively.

By comparing with the theoretical MCBR model expectations, these trends may be interpreted as follows: the early stage with positive slope may safely be related to assembling (A), the middle stage with nearly flat

Table 7: Regression line slope and intercept estimators,  $\hat{\alpha}_O$  and  $\hat{\beta}_O$ , and related dispersion estimators,  $\hat{\sigma}_{\hat{\alpha}_O}$ , and  $\hat{\sigma}_{\hat{\beta}_O}$ , for regression models applied to the oxygen empirical differential abundance distribution (EDAD) plotted in Fig. 4, related to different regions (reg). The method has dealt with each stage (S) separately: A - assembling, F - formation, E - evolution. A single stage (E) has been considered for halo population due to the incompleteness of related subsample. Bins containing a single star are not considered in the regression.

S	$\hat{\alpha}_O$	$\hat{\sigma}_{\hat{\alpha}_O}$	$\hat{\beta}_O$	$\hat{\sigma}_{\hat{\beta}_O}$	reg
A	+3.2643 E-0	1.8045 E-0	-1.4001 E-0	5.0690 E-1	KD
A	+2.3871 E-0	7.5607 E-1	-1.4681 E-0	4.2787 E-1	ND
A	+3.9590 E-0	1.0948 E-0	-2.0445 E-0	3.3269 E-1	DD
F	+1.9851 E-1	4.4600 E-3	-6.4657 E-2	2.7360 E-3	KD
F	+2.0642 E-1	1.3444 E-1	-1.4400 E-1	1.1628 E-1	ND
F	+1.6397 E-2	1.2453 E-2	+1.2886 E-2	9.6177 E-3	DD
E	-1.2001 E-0	1.0914 E-1	+1.0764 E-0	1.2480 E-1	KD
E	-1.4891 E-0	1.8978 E-1	+1.6313 E-0	2.3646 E-1	ND
E	-1.5392 E-0	8.5043 E-2	+1.6397 E-0	1.2252 E-1	DD
E	-1.8764 E-0	3.0416 E-1	+8.1914 E-1	1.1220 E-1	HH

Table 8: Regression line slope and intercept estimators,  $\hat{\alpha}_{\text{Fe}}$  and  $\hat{\beta}_{\text{Fe}}$ , and related dispersion estimators,  $\hat{\sigma}_{\hat{\alpha}_{\text{Fe}}}$ , and  $\hat{\sigma}_{\hat{\beta}_{\text{Fe}}}$ , for regression models applied to the iron empirical differential abundance distribution (EDAD) plotted in Fig. 5, related to different regions (reg). The method has dealt with each stage (S) separately: A - assembling, F - formation, E - evolution. A single stage (E) has been considered for halo population due to the incompleteness of related subsample. For KD subsample, stages F and E are also considered as a single stage, FE. Bins containing a single star are not considered in the regression.

S	$\hat{\alpha}_{\text{Fe}}$	$\hat{\sigma}_{\hat{\alpha}_{\text{Fe}}}$	$\hat{\beta}_{\text{Fe}}$	$\hat{\sigma}_{\hat{\beta}_{\text{Fe}}}$	reg
A	+6.9323 E-0	3.2108 E-0	-8.2705 E-1	4.5176 E-1	KD
A	+4.1103 E-0	5.0477 E-1	-1.5270 E-0	1.7900 E-1	ND
A	+7.5777 E-0	3.3920 E-0	-1.4135 E-0	4.8156 E-1	DD
F	-4.8416 E-1	7.8092 E-1	+3.5966 E-1	1.9595 E-1	KD
F	-2.5801 E-1	1.1309 E-1	+1.7609 E-1	8.4070 E-2	ND
F	-1.6209 E-1	1.2974 E-1	+2.9866 E-2	8.5168 E-2	DD
E	-9.5208 E-1	4.8752 E-2	+4.8016 E-1	4.3781 E-2	KD
E	-1.3329 E-0	1.0979 E-1	+1.2826 E-0	1.4090 E-1	ND
E	-1.2115 E-0	7.2617 E-2	+1.0469 E-0	9.5796 E-2	DD
E	-3.1707 E-0	8.8934 E-1	+1.0858 E-0	1.4100 E-1	HH
FE	-9.3301 E-1	4.2058 E-2	+4.5619 E-1	3.3064 E-2	KD

Table 9: Transition (trans) points between adjacent stages, as determined from the intersection of related regression lines,  $(\phi_Q, \psi_Q)$ ,  $Q = O, Fe$ , for the empirical differential abundance distribution (EDAD) plotted in Figs. 4-5, respectively, with regard to HH, KD, ND, DD subsample (sub). For KD subsample, stages F and E are also considered as a single stage, FE, with regard to iron. Regression lines outside the domain of subsample abundance, denoted as stage O, are assumed to be vertical lines.

trans	$\phi_O$	$\psi_O$	$\phi_{Fe}$	$\psi_{Fe}$	sub
O-E	2.2387 E-2	+7.7714 E-1	4.4668E-2	+9.4414E-1	HH
E-O	8.9125 E-1	-8.5318 E-1	3.5481E-1	-3.9241E-1	HH
O-A	1.7783 E-1	-8.1960 E-1	5.6234E-2	-4.3722E-1	KD
A-F	4.3559 E-1	+2.1810 E-2	1.6001E-1	+2.8219E-1	KD
F-E	8.1590 E-1	+9.7304 E-2	2.5752E-1	+2.3498E-1	KD
E-O	2.2387 E-0	-1.6102 E-0	2.8184E-0	-2.2032E-0	KD
A-FE			1.6315E-1	+3.0397E-1	KD
O-A	2.8184 E-1	-7.9533 E-1	1.4125E-1	-9.4641E-1	ND
A-F	6.0720 E-1	-1.8662 E-2	3.8987E-1	+7.5496E-2	ND
F-E	1.0470 E-0	+1.2229 E-1	1.0294E-0	-9.6202E-2	ND
E-O	2.8184 E-0	-2.5657 E-0	2.8184E-0	-2.4742E-0	ND
O-A	1.7783 E-1	-1.3404 E-0	5.6234E-2	-9.8735E-1	DD
A-F	5.2182 E-1	+2.1442 E-2	1.8648E-1	-3.6075E-4	DD
F-E	1.0458 E-0	+3.0034 E-2	9.6920E-1	-1.3351E-1	DD
E-O	2.8184 E-0	-2.5252 E-0	2.8184E-0	-2.3674E-0	DD

slope to formation (F), the late stage with negative slope to evolution (E). The last stage could be in connection with different trends implying two fitting straight lines which, in general, form a knee.

In this view, A stage is characterized by SI inflow regime, F stage by SS inflow regime, E stage by WI inflow (to be intended as including outflow) regime, as shown in Fig. 4 for oxygen EDAD. Iron EDAD exhibits a similar trend with respect to oxygen and, in addition, a peak related to F stage, as shown in Fig. 5. If delayed recycling via SNIa progenitors is the main process which makes iron np element, then the above mentioned peak can be related to the onset of SNIa events.

In summary, the following informations can be inferred from oxygen and iron EDAD via Table 9: (i) the transition from SI to SS inflow regime took place at  $[O/H] \approx -0.36$  for the thick disk and  $[O/H] \approx -0.22$  for the thin disk; the transition from SS to WI inflow regime took place at  $[O/H] \approx -0.09$  for the thick disk and  $[O/H] \approx +0.02$  for the thin disk; (ii) the onset of SNIa events took place at  $[Fe/H] \approx -0.80$  for the thick disk and  $[Fe/H] \approx -0.40$  for the thin disk. No conclusion can be drawn for the halo, due to the incompleteness of related subsample.

With regard to KD subsample, oxygen EDAD shows a similar trend to the one found in an earlier investigation (Caimmi 2012a) for a sample of 133 thick disk stars from Ramírez et al. (2007). However, when we compare the present results with those from C13b, obtained with the sample of Ramírez et al. (2012), we see that, while iron EDAD exhibits a similar trend to that one, within the common abundance range, the contrary holds for oxygen EDAD. More specifically, fitting straight lines within the common abundance range ( $[O/H] < -0.05$ ) show a negative slope instead of positive or close to zero as outlined in Fig. 4, top right panel ( $\phi_O < 0.9$ ). The above mentioned discrepancy is probably owing to the combined effect of poor subsample (16 stars compared with the 133 from Ramírez et al. 2007), biases against high iron abundance, larger oxygen abundance scatter with respect to iron abundance.

### 4.1.3 Nonlinear iron TDAD

Let Q be a selected element for which both the empirical  $[Q/H]$ - $[O/H]$  relation:

$$[Q/H] = a_Q [O/H] + b_Q ; \quad (12)$$

and oxygen EDAD have been inferred from a selected star sample. Using the relation between number abundance and mass abundance (e.g., Caimmi

2007; C13b):

$$\log \frac{\phi_Q}{\phi_H} = [Q/H] \quad ; \quad (13)$$

after little algebra Eq. (12) translates into:

$$\phi_Q = B_Q \phi_H^{1-a_Q} \phi_O^{a_Q} \quad ; \quad B_Q = \exp_{10}(b_Q) \quad ; \quad (14)$$

where  $\phi_H$  is the hydrogen abundance normalized to the solar value, which is expected to change only slightly in time and may safely be assumed as constant. Accordingly, a differentiation on both sides of Eq. (14) yields:

$$d\phi_Q = B_Q a_Q \left( \frac{\phi_O}{\phi_H} \right)^{a_Q-1} d\phi_O \quad ; \quad (15)$$

where  $d\phi_Q$  and  $d\phi_O$  may be conceived as infinitely thin bins centered on  $\phi_Q$  and  $\phi_O$ , respectively, both containing an equal infinitesimal number of stars,  $dN$ .

Finally, the TDAD of the element, Q, may be expressed as:

$$\psi_Q = \log \left( \frac{dN}{N d\phi_Q} \right) = \log \left( \frac{dN}{N d\phi_O} \frac{d\phi_O}{d\phi_Q} \right) = \psi_O + \log \left( \frac{d\phi_O}{d\phi_Q} \right) \quad ; \quad (16)$$

and the substitution of Eqs. (8) and (15) into (16) after some algebra yields:

$$\psi_Q = \alpha_O \phi_O + \beta_O - b_Q - \log a_Q - (a_Q - 1) \log \left( \frac{\phi_O}{\phi_H} \right) \quad ; \quad (17)$$

which, in terms of Q abundance, by use of Eq. (14), after some algebra translates into:

$$\psi_Q = \alpha_Q \left( \frac{\phi_Q}{\phi_H} \right)^{1/a_Q} \phi_H + \beta_Q - (a_Q - 1) \log \left( \frac{\phi_Q}{\phi_H} \right)^{1/a_Q} \quad ; \quad (18)$$

$$\alpha_Q = \frac{\alpha_O}{B_Q^{1/a_Q}} \quad ; \quad \beta_Q = \beta_O - \log a_Q - \frac{b_Q}{a_Q} \quad ; \quad (19)$$

where hydrogen abundance,  $\phi_H$ , may safely be put equal to unity. If the element, Q, is sp,  $a_Q = 1$ , then Eq. (18) reduces to (8).

The special case of iron, related to HH, KD, ND, DD subsamples, is plotted in Fig. 6 using the results listed in Tables 3 and 7, and compared with its empirical counterpart shown in Fig. 5. The SS inflow regime, inferred from oxygen EDAD via Eq. (14), is marked by dotted vertical lines. An inspection

of Fig. 6 shows iron TDAD, expressed by Eq. (18) where  $Q = \text{Fe}$ ,  $\phi_{\text{H}} = 1$ , and the values of coefficients are inferred from Tables 3 and 7 via Eq. (19), can be approximated, to a first extent, by regression lines to iron EDAD for different inflow regimes, shown in Fig. 5. Therefore simple MCBR chemical evolution models may safely be used for the description of iron chemical evolution, with regard to subsamples under consideration.

#### 4.1.4 Inflow/outflow rate for different populations

With regard to oxygen, which may safely be conceived as sp element within the framework of simple MCBR chemical evolution models, the assumption of universal stellar IMF implies constant oxygen yield,  $\hat{p}_{\text{O}}$ , for different populations. Though products of stellar nucleosynthesis vary with the initial metallicity (e.g., Woosley and Weaver 1995), still oxygen and iron yields per star generation show a mild dependence (e.g., Yates et al. 2013) which can be neglected to a first extent.

Accordingly, the following relation (C13b) is easily inferred from Eq. (10):

$$\frac{(\alpha_{\text{O}})_{\text{XY}}}{(\alpha_{\text{O}})_{\text{WZ}}} = \frac{1 + \kappa_{\text{XY}}}{1 + \kappa_{\text{WZ}}} ; \quad (20)$$

where  $\kappa$  is the flow parameter, proportional to inflow ( $\kappa < 0$ ) or outflow ( $\kappa > 0$ ) rate, as explained, and XY, WZ, identify subsamples under consideration. For constant effective yield,  $\hat{p}_{\text{O}}/(1 + \kappa)$ , i.e. constant flow parameter,  $\kappa$ , the  $\alpha_{\text{O}}$  ratio related to different regions remains unchanged. Then  $\alpha_{\text{O}}$  ratios different from unity imply different inflow or outflow rate for different regions.

Oxygen TDAD slopes,  $\alpha_{\text{O}}$ , are inferred from the data, which implies constraints on flow parameters related to different environments, via Eq. (20). Keeping in mind regression lines exhibit slope of equal sign for a selected stage, as shown in Table 7, Eq. (20) discloses that related flow parameters must be both larger/lower than or equal to  $-1$ , which implies the additional condition,  $(\alpha_{\text{O}})_{\text{XY}}/(\alpha_{\text{O}})_{\text{WZ}} > 0$ , holds for a selected stage according to the results listed in Table 7. Little algebra shows the correlation between slope ratio and flow parameter ratio, for assigned values of  $\kappa_{\text{WZ}}$ , as:

$$\frac{(\alpha_{\text{O}})_{\text{XY}}}{(\alpha_{\text{O}})_{\text{WZ}}} \lesseqgtr 1 ; \quad \frac{\kappa_{\text{XY}}}{\kappa_{\text{WZ}}} \lesseqgtr 1 ; \quad \kappa_{\text{WZ}} \leq -1 ; \quad \kappa_{\text{WZ}} \geq 0 ; \quad (21\text{a})$$

$$\frac{(\alpha_{\text{O}})_{\text{XY}}}{(\alpha_{\text{O}})_{\text{WZ}}} \lesseqgtr 1 ; \quad \frac{\kappa_{\text{XY}}}{\kappa_{\text{WZ}}} \gtrless 1 ; \quad -1 \leq \kappa_{\text{WZ}} \leq 0 ; \quad (21\text{b})$$

which have to be read taking into consideration both lower (first alternative) and upper (second alternative) inequalities, where the equality (third

Table 10: Oxygen regression line slope ratio,  $s_O = (\alpha_O)_{XY}/(\alpha_O)_{WZ}$ , and flow parameters,  $\kappa_{WZ}$ , inferred from Eq. (20) for a reference value,  $\kappa_{HH} = 10$ , with regard to different subsamples, XY, WZ; XY = ND, HH; WZ = KD, ND, DD; and different inflow regime (IR), strong inflow (SI), steady state inflow (SS), weak inflow or outflow (WI). The reference value assumed for the flow parameter is valid only in WI regime. See text for further details.

IR	$s_O$	$\kappa_{WZ}$	XY	WZ
SI	0.7313		ND	KD
SS	1.0399		ND	KD
WI	1.2409		ND	KD
	1.5636	6.0350	HH	KD
	1.2600	7.7302	HH	ND
	1.2191	8.0230	HH	DD

alternative) separates the two above. The limit of dominant inflow/outflow rate,  $|\kappa| \gg 1$ , for both XY and WZ subsamples, implies  $(\alpha_O)_{XY}/(\alpha_O)_{WZ} \approx \kappa_{XY}/\kappa_{WZ}$  to a good extent.

Then the knowledge of oxygen TDAD fractional slopes,  $s_O = (\alpha_O)_{XY}/(\alpha_O)_{WZ}$ , quantifies restrictions on the flow parameter ratio,  $\kappa_{XY}/\kappa_{WZ}$ . Oxygen TDAD fractional slopes are listed in Table 10 for different inflow regimes (IR) and different subsamples (XY, WZ). The results presented in Tables 7 and 10 disclose that oxygen regression line slope ratios are consistent with unity within  $\mp \hat{\sigma}_{\hat{\alpha}}$  for disk populations and within  $\mp 2\hat{\sigma}_{\hat{\alpha}}$  for disk and halo populations.

Accordingly, inflow rate of comparable extent took place within the thick and the thin disk during SI inflow regime ( $\kappa \ll -1$ ), with a difference not exceeding a factor of about 1.3. The same holds for SS inflow regime, in that a null slope of the regression line relates to  $\kappa = -1$  (Caimmi 2011a) and the slopes considered are slightly larger than zero, which implies flow parameters slightly lower than negative unity, as shown above.

Concerning WI inflow regime, outflow rate could be conceived as strong for halo population, with a reference flow parameter value,  $\kappa_{HH} = 10$  (e.g., Hartwick 1976), which via Eq. (20) yields lower values for the disk population, but within the same order of magnitude, as shown in Table 10. On the other hand, substantial gas outflow from the disk could be avoided if (i) the HH subsample is representative of the inner halo and (ii) strong outflow rate relates to the outer halo, which exhibits different trends with respect to the inner halo in both kinematics and chemical composition (e.g., Carollo et al. 2007, 2010). The above considerations hold within the framework of

simple MCBR chemical evolution models, which imply (among others) the assumption of instantaneous mixing.

In the special case where sample stars belong to a single generation, when all stars have a similar abundance for O and Fe, an EDAD different to a delta function could only be due to cosmic scatter. This is, of course, excluded for the thin disk, where star formation is currently going on, but should be considered for both the thick disk and the halo, which host old populations only.

If the cosmic scatter obeys a lognormal distribution, where the mean and the variance can be evaluated from the data, the TDAD reads (C13a; C13b):

$$(\psi)_{cs} = \log \left\{ \frac{1}{\ln 10} \frac{1}{\sqrt{2\pi}\sigma_Q} \exp \left[ -\frac{(\log \phi_Q - \overline{\log \phi_Q})^2}{2\sigma_Q^2} \right] \frac{1}{\phi_Q} \right\} ; \quad (22)$$

where the index, cs, denotes cosmic scatter,  $\overline{\log \phi_Q} = \overline{[Q/H]}$  and  $\sigma_Q = \sigma_{[Q/H]}$ . Related curves, expressed by Eq. (22), are plotted in Figs. 4-5 as full curves, for Q = O, Fe, with regard to ND, KD, DD, HH subsamples, from top left in clockwise sense. To this aim, the values listed in Table 6 have been used. An inspection of Figs. 4-5 shows both oxygen and iron EDAD cannot be due to cosmic scatter for disk population, as expected for the thin disk, while it remains a viable alternative for halo population provided HH subsample can be considered as representative.

#### 4.1.5 Evolution of the thick disk

According to recent investigations (Haywood et al. 2013; Snaith et al. 2014), the history of the thick disk was characterized by high star formation efficiency, yielding a global mass comparable to the amount of the thin disk. In particular, the inferred star formation rate (Snaith et al. 2014, Fig. 2b) relates to three different stages which, by analogy with three different stages related to oxygen EDAD, can be similarly defined here as: A ( $13.5 \gtrsim t_{lb}/\text{Gyr} \gtrsim 12.5$ ); F ( $12.5 \gtrsim t_{lb}/\text{Gyr} \gtrsim 9.5$ ); E ( $9.5 \gtrsim t_{lb}/\text{Gyr} \gtrsim 8.0$ ); where  $t_{lb}$  is the lookback time and star formation within the thick disk is assumed to end at  $t_{lb}/\text{Gyr} \approx 8.0$ .

Within the framework of simple MCBR models, the transition between different stages takes place at  $\phi_{\text{Fe}} \approx 0.2$  and  $\phi_{\text{Fe}} \approx 0.5$  (Fig. 6, top right panel) or  $[\text{Fe}/\text{H}] \approx -0.70$  and  $[\text{Fe}/\text{H}] \approx -0.30$ , respectively. By use of the inferred  $[\text{Si}/\text{Fe}]$ - $[\text{Fe}/\text{H}]$  relation (Snaith et al. 2014, Fig. 2d), the above mentioned values relate to  $[\text{Si}/\text{Fe}] \approx 0.22$  and  $[\text{Si}/\text{Fe}] \approx 0.15$ , respectively which, in turn, via the inferred  $[\text{Si}/\text{Fe}]$ -age relation (Snaith et al. 2014, Fig. 2a) correspond to  $t_{lb}/\text{Gyr} \approx 12.5$  and  $t_{lb}/\text{Gyr} \approx 10.0$ , respectively.

Table 11: Normalization constant,  $(C_U)_N$ , flow parameter,  $\kappa_U$ , active gas mass fraction,  $(\mu_U)_f$ , star mass fraction,  $(s_U)_f$ , inflowed or outflowed gas mass fraction,  $(D_U)_f$ , inferred from simple MCBR models related to the thick disk (Fig. 4, top right panel). See text for further details.

U	$(C_U)_N$	$\kappa_U$	$(\mu_U)_f$	$(s_U)_f$	$(D_U)_f$
A	1.1974E-1	-8.7722E-0	6.9409E-0	7.6437E-1	-6.7052E+0
F	5.5650E-1	-1.4726E-0	8.2586E-0	3.5525E-0	-1.0811E+1
E	1.0004E-0	+1.8573E-0	1.6196E-1	6.3862E-0	-5.5481E+0

The chemical evolution of the thick disk can be inferred from oxygen EDAD via simple MCBR models. The results are listed in Table 11, with regard to the normalization constant for matching oxygen TDAD with related EDAD,  $(C_U)_N$ , the flow parameter,  $\kappa_U$ , the active (i.e. available for star formation) gas mass fraction,  $(\mu_U)_f$ , the star mass fraction,  $(s_U)_f$ , the inflowed or outflowed gas mass fraction,  $(D_U)_f$ , where mass fractions are related to the initial total mass, assumed to be entirely gaseous,  $\mu_i = 1$ , and the index, f, marks the end of each stage, U = A, F, E. For further details, an interested reader is addressed to earlier attempts where MCBR models are formulated (Caimmi 2011a, 2012a).

An inspection of Table 11 shows a net gas inflow larger than the initial mass by a factor of about 10.8, and a final star mass fraction of about 6.39, slightly larger than a final active + outflowed gas mass fraction of about 5.71. Accordingly, the thick and the thin disk are comparable in mass provided the thin disk was built up from the gas left after thick disk formation, as suggested in recent investigations (Haywood et al. 2013; Snaith et al. 2014). In addition, the flow parameter,  $\kappa_U$ , equals (in absolute value) about 8.77 in strong inflow regime, U = A; about 1.47 in (nearly) steady state inflow regime, U = F; about 1.86 in outflow regime, U = E.

Within the framework of simple MCBR models yielding the results listed in Table 11, the history of the thick disk can be inferred from the above mentioned findings (Haywood et al. 2013; Snaith et al. 2014) as follows.

- (1) A short (about 1.0 Gyr) stage in strong inflow ( $\kappa_A \approx -8.77$ ) regime, where the active gas and the star mass fraction (with respect to the initial mass) grow up to  $(\mu_A)_f \approx 6.94$  and  $(s_A)_f \approx 0.76$ , respectively.
- (2) A long (about 2.5 Gyr) stage in (nearly) steady state inflow ( $\kappa_A \approx -1.47$ ) regime, where the active gas and the star mass fraction grow

up to  $(\mu_F)_f \approx 8.26$  and  $(s_F)_f \approx 3.55$ , respectively.

- (3) A medium (about 1.5 Gyr) stage in outflow ( $\kappa_A \approx 1.86$ ) regime, where the active gas mass fraction decreases down to  $(\mu_E)_f \approx 0.16$  and the star mass fraction grows up to  $(s_E)_f \approx 6.39$ , respectively.

If the global gas mass fraction left at the end of thick disk evolution,  $(\mu_E)_f + (D_E)_f \approx 5.71$ , is used for building up the thin disk, assuming  $(M_{\text{thin}})_f = 5.71 \cdot 10^{10} m_\odot$  for simplicity, then the initial thick disk mass amounts to  $(M_{\text{thick}})_i = 10^{10} m_\odot$ , which grows up to  $(M_{\text{thick}})_f = 6.39 \cdot 10^{10} m_\odot$  at the end of evolution, comparable to thin disk mass, as suggested in recent attempts (Haywood et al. 2013; Snaith et al. 2014).

## 4.2 Yields and yield ratios

### 4.2.1 Iron production via sp and np processes

Let Q be a selected element for which the empirical  $[Q/H]$ - $[O/H]$  relation has been linearly fitted according to Eq. (12). If only the contribution of sp processes is taken into consideration, Eq. (12) reduces to:

$$[Q_{\text{sp}}/H] = [O/H] + b_{Q_{\text{sp}}} ; \quad (23)$$

where oxygen may be thought of as sp element to a good extent.

By use of Eq. (13), after little algebra Eq. (23) translates into:

$$\phi_{Q_{\text{sp}}} = B_{Q_{\text{sp}}} \phi_O ; \quad B_{Q_{\text{sp}}} = \exp_{10}(b_{Q_{\text{sp}}}) ; \quad (24)$$

which, together with Eq. (14), implies the following:

$$\frac{\phi_{Q_{\text{sp}}}}{\phi_Q} = \frac{B_{Q_{\text{sp}}}}{B_Q} \left( \frac{\phi_O}{\phi_H} \right)^{1-a_Q} ; \quad (25)$$

$$\frac{\phi_{Q_{\text{np}}}}{\phi_Q} = 1 - \frac{\phi_{Q_{\text{sp}}}}{\phi_Q} ; \quad (26)$$

where  $\phi_{Q_{\text{np}}}$  is the amount of the element, Q, produced via np processes.

The particularization of Eq. (25) to the minimum abundance exhibited by subsample stars, denoted by the index,  $m$ , yields:

$$\left( \frac{\phi_{Q_{\text{sp}}}}{\phi_Q} \right)_m = \frac{B_{Q_{\text{sp}}}}{B_Q} \left[ \left( \frac{\phi_O}{\phi_H} \right)_m \right]^{1-a_Q} ; \quad (27)$$

where both  $(\phi_{Q_{\text{sp}}})_m$  and  $B_{Q_{\text{sp}}}$  are unknown while the remaining quantities can be inferred from the data. For sufficiently old and low-metallicity stars,

as it is in the case under consideration, the abundance fraction,  $(\phi_{\text{Qsp}}/\phi_{\text{Q}})_m$ , may safely be put equal to unity. Accordingly, Eq. (27) reduces to:

$$\frac{B_{\text{Qsp}}}{B_{\text{Q}}} = \left[ \left( \frac{\phi_{\text{O}}}{\phi_{\text{H}}} \right)_m \right]^{a_{\text{Q}}-1} ; \quad (28)$$

and the substitution of Eq. (28) into (25) after some algebra yields:

$$\frac{\phi_{\text{Qsp}}}{\phi_{\text{Q}}} = \left[ \frac{\phi_{\text{O}}/(\phi_{\text{O}})_m}{\phi_{\text{H}}/(\phi_{\text{H}})_m} \right]^{1-a_{\text{Q}}} ; \quad (29)$$

finally, the substitution of Eq. (28) into (24) produces:

$$\phi_{\text{Qsp}} = B_{\text{Q}} \left[ \left( \frac{\phi_{\text{O}}}{\phi_{\text{H}}} \right)_m \right]^{a_{\text{Q}}-1} \phi_{\text{O}} ; \quad (30)$$

which, on the  $(\text{O}\phi_{\text{O}}\phi_{\text{Q}})$  plane, represents a straight line passing through the origin and the point,  $[(\phi_{\text{O}})_m, (\phi_{\text{Q}})_m]$ .

The special case of iron, related to HH, KD, ND, DD subsamples, taking  $\phi_{\text{H}} = 1$  (which implies hydrogen abundance in long-lived stellar atmospheres changes only slightly with respect to the sun), is plotted in Fig. 7 for both global (full curves) and partial (sp - dashed curves; np - dotted curves) abundances. The abundance range related to the SS inflow regime inferred from oxygen EDAD, plotted in Fig. 4, is marked by dotted vertical lines. An asterisk on the global abundance curve denotes the peak of iron EDAD shown in Fig. 5.

An inspection of Fig. 7 discloses that iron production via sp and np processes is comparable, leaving aside lower abundances, for HH ( $\phi_{\text{O}} < 3$ ), KD ( $\phi_{\text{O}} < 1$ ), ND ( $1 < \phi_{\text{O}} < 3$ ), DD ( $\phi_{\text{O}} < 1$ ) subsample, while the contrary holds for higher abundances exceeding the above mentioned thresholds.

The assumption of minimum subsample star abundance entirely related to sp processes,  $(\phi_{\text{Fe,sp}})_m = (\phi_{\text{Fe}})_m$ , allows an explicit expression of  $B_{\text{Qsp}}$ , Eq. (28), and then  $\phi_{\text{Qsp}}$ , Eq. (29). Alternatively, the following working hypotheses can be made: (a) the above assumption, which implies the validity of Eqs. (28)-(29), is restricted to the thick disk, where stars are globally older and metal poorer than in other disk subsamples, and (b) the  $\phi_{\text{Qsp}} - \phi_{\text{O}}$  relation, expressed by Eq. (24), is universal i.e.  $B_{\text{Qsp}}$  has the same value regardless of the population, in particular it can be inferred from Eqs. (28)-(29) related to the thick disk. Accordingly, dashed lines plotted in Fig. 7 would be changed into their counterpart related to the thick disk.

Then the minimum subsample (XY) star fractional abundance contributed by sp processes,  $\left[ (\phi_{\text{Qsp}}/\phi_{\text{Q}})_m \right]_{\text{XY}}$ , can be explicitly written via the following steps.

- (i) Particularize Eq. (24) to minimum subsample star abundances and infer  $\left[\left(\phi_{\text{Q}_{\text{sp}}}/\phi_{\text{Q}}\right)_m\right]_{\text{XY}}$ .
- (ii) Substitute  $B_{\text{Q}_{\text{sp}}}$  therein by use of Eq. (28).
- (iii) Particularize Eq. (14) to minimum subsample star abundances and infer  $\left[\left(\phi_{\text{Q}}/\phi_{\text{O}}\right)_m\right]_{\text{XY}}$ .
- (iv) Substitute  $\left[\left(\phi_{\text{Q}}/\phi_{\text{O}}\right)_m\right]_{\text{XY}}$  into the above expression of  $\left[\left(\phi_{\text{Q}_{\text{sp}}}/\phi_{\text{Q}}\right)_m\right]_{\text{XY}}$ .

The result is:

$$\left[\left(\frac{\phi_{\text{Q}_{\text{sp}}}}{\phi_{\text{Q}}}\right)_m\right]_{\text{XY}} = \frac{(B_{\text{Q}})_{\text{KD}} \left\{ \left[ \left( \phi_{\text{O}}/\phi_{\text{H}} \right)_m \right]_{\text{KD}} \right\}^{(a_{\text{Q}})_{\text{KD}} - 1}}{(B_{\text{Q}})_{\text{XY}} \left\{ \left[ \left( \phi_{\text{O}}/\phi_{\text{H}} \right)_m \right]_{\text{XY}} \right\}^{(a_{\text{Q}})_{\text{XY}} - 1}} ; \quad (31)$$

where  $\text{XY} = \text{HH}, \text{ND}, \text{DD}$ , and  $\text{XY} = \text{KD}$  yields the unit value, as expected.

In the case under consideration,  $\text{Q} = \text{Fe}$  and  $\phi_{\text{H}} \approx 1$  may safely be assumed, as hydrogen abundance in long-lived stellar atmospheres is expected to remain more or less unchanged with respect to solar abundance. Some results are listed in Table 12, where  $\phi_{\text{O}}$  is directly inferred from related subsample;  $\phi_{\text{Fe}}$  and  $d\phi_{\text{Fe}}/d\phi_{\text{O}}$  are calculated via Eq. (14);  $\phi_{\text{Fe}_{\text{sp}}}/\phi_{\text{Fe}}$  is calculated via Eq. (31); where all values hold for both the alternatives discussed above with the exception of the last one, which is restricted to the second alternative. It is worth noticing comparable  $(d\phi_{\text{Fe}}/d\phi_{\text{O}})_m$  values are shown for HH and KD subsamples, and comparable  $(d\phi_{\text{Fe}}/d\phi_{\text{O}})_M$  values for KD and ND subsamples, in connection with a reference maximum oxygen abundance,  $(\phi_{\text{O}})_M = 3$ .

#### 4.2.2 Iron-to-oxygen yield ratio

With regard to Fig. 6, the iron-to-oxygen yield ratio can be expressed in terms of either iron-to-oxygen normalized abundance ratio,  $\phi_{\text{Fe}}/\phi_{\text{O}}$ , via Eq. (2), or slope ratio of regression lines related to a selected inflow regime for both oxygen and iron EDAD, respectively,  $(\alpha_{\text{O}})_{\text{IR}}/(\alpha_{\text{Fe}})_{\text{IR}}$ , via Eq. (10), as (C13b):

$$\frac{\hat{p}_{\text{Fe}}}{\hat{p}_{\text{O}}} = \frac{(Z_{\text{Fe}})_{\odot} \phi_{\text{Fe}}}{(Z_{\text{O}})_{\odot} \phi_{\text{O}}} ; \quad (32)$$

$$\frac{\hat{p}_{\text{Fe}}}{\hat{p}_{\text{O}}} = \frac{(Z_{\text{Fe}})_{\odot} (\alpha_{\text{O}})_{\text{IR}}}{(Z_{\text{O}})_{\odot} (\alpha_{\text{Fe}})_{\text{IR}}} ; \quad (33)$$

where  $\text{IR} = \text{SI}, \text{SS}, \text{WI}$ , denotes the inflow regime.

Table 12: Minimum subsample (sub) oxygen abundance,  $(\phi_{\text{O}})_m$ , and inferred iron abundance,  $(\phi_{\text{Fe}})_m$ , related fractional iron abundance due to sp processes,  $(\phi_{\text{Fe}_{\text{sp}}}/\phi_{\text{Fe}})_m$ , and slope of  $\phi_{\text{Fe}}-\phi_{\text{O}}$  relation,  $(d\phi_{\text{Fe}}/d\phi_{\text{O}})_m$ , with the addition of its counterpart,  $(d\phi_{\text{Fe}}/d\phi_{\text{O}})_M$ , for a reference maximum oxygen abundance,  $(\phi_{\text{O}})_M = 3$ . Iron abundances and slopes are determined via Eq. (14). Fractional iron abundances are determined under the assumption of universal  $\phi_{\text{Fe}_{\text{sp}}}-\phi_{\text{O}}$  relation, according to Eq. (31), with a unit value related to the lowest slope (KD subsample). See text for further details.

$(\phi_{\text{O}})_m$	$(\phi_{\text{Fe}})_m$	$(\phi_{\text{Fe}_{\text{sp}}}/\phi_{\text{Fe}})_m$	$(d\phi_{\text{Fe}}/d\phi_{\text{O}})_m$	$(d\phi_{\text{Fe}}/d\phi_{\text{O}})_M$	sub
2.52855D-2	7.89204D-3	7.20182D-1	3.665260D-1	8.427390D-1	HH
1.59541D-1	3.58617D-2	1	3.599973D-1	2.102907D-0	KD
3.18326D-1	1.77952D-1	3.98951D-1	7.635178D-1	1.734610D-0	ND
1.59541D-1	4.30047D-2	8.33903D-1	4.297271D-1	2.456852D-0	DD

In particular, SS inflow regime relates to regression lines with slopes close to zero, as shown in Figs. 4 and 5, which implies slopes with different sign for oxygen and iron, though consistent within the errors, as shown in Tables 7 and 8. On the other hand, the yield ratio has to be non negative in the case under discussion, which implies Eq. (33) is physically meaningless or, in other words, the yield ratio cannot be inferred via Eq. (33) for SS inflow regime.

The substitution of Eq. (14), particularized to  $Q = \text{Fe}$ , into Eq. (32) after little algebra yields:

$$\frac{\hat{p}_{\text{Fe}}}{\hat{p}_{\text{O}}} = \frac{(Z_{\text{Fe}})_{\odot}}{(Z_{\text{O}})_{\odot}} B_{\text{Fe}} \left( \frac{\phi_{\text{O}}}{\phi_{\text{H}}} \right)^{a_{\text{Fe}}-1} ; \quad (34)$$

which depends on oxygen-to-hydrogen abundance ratio. With regard to a selected inflow regime, the combination of Eqs. (33) and (34) produces:

$$b_{\text{Fe}} = \log B_{\text{Fe}} = \log \left[ \frac{(\alpha_{\text{O}})_{\text{IR}}}{(\alpha_{\text{Fe}})_{\text{IR}}} \right] - (a_{\text{Fe}} - 1) \log \left( \frac{\phi_{\text{O}}}{\phi_{\text{H}}} \right) ; \quad (35)$$

which, keeping in mind  $b_{\text{Fe}}$  is inferred from the  $[\text{Fe}/\text{H}]-[\text{O}/\text{H}]$  empirical relation, discloses the extent to which iron TDAD, plotted in Fig. 5, fits to its counterpart, depending on oxygen abundance, plotted in Fig. 6.

Leaving aside F stage, where oxygen and iron regression lines show small but opposite slopes,  $(\alpha_{\text{O}})_{\text{SS}} > 0$ ,  $(\alpha_{\text{Fe}})_{\text{SS}} < 0$ , and Eq. (35) is undefined,

marginal disagreement, marginal agreement, satisfactory agreement are found for KD, DD, ND and HH subsamples, respectively. In other words, iron TDAD plotted in Fig. 5 is marginally inconsistent, marginally consistent, satisfactorily consistent with the empirical [Fe/H]-[O/H] relation for KD, DD, ND and HH subsamples, respectively, even if they fit to related EDAD in all cases.

The yield ratio,  $\hat{p}_{\text{Fe}}/\hat{p}_{\text{O}}$ , expressed by Eq. (34), as a function of iron abundance,  $\phi_{\text{Fe}}$ , is plotted in Fig. 8 for ND, KD, DD, HH subsample (from top left in clockwise sense), where different stages are marked by dotted vertical lines, as in Fig. 6. Yields ratios inferred from EDAD regression lines are represented on related curves as asterisks for both A (left) and E (right) stage, with no connection with iron abundance.

Theoretical yield ratios for a power-law IMF with exponent,  $-p = -2$  (down) and  $-p = -3$  (up), restricted to  $9 \leq m/m_{\odot} \leq 20$ , are also shown for different initial metal abundance,  $Z = 0.0004$  (crosses),  $0.004$  (diamonds),  $0.008$  (triangles),  $0.02$  (squares),  $0.05$  (saltires), as inferred from an earlier research (Portinari et al. 1998) under the restriction,  $Z_{\text{Fe}}/Z = (Z_{\text{Fe}})_{\odot}/Z_{\odot}$ , unless initial iron abundance used for the stellar evolution is known.

Lower values, by a factor not exceeding about two, are obtained in connection with the following mass ranges:  $12 \leq m/m_{\odot} \leq 20$ ,  $9 \leq m/m_{\odot} \leq 30$ ,  $12 \leq m/m_{\odot} \leq 30$ ,  $9 \leq m/m_{\odot} \leq 120$ . For further details on the stellar mass range related to oxygen production and additional references, an interested reader is addressed to a recent research (Acharova et al. 2013) where, in particular, an upper mass limit for SNII progenitors within the range,  $19 \lesssim m/m_{\odot} \lesssim 32$ , with a preferred value,  $m \approx 23m_{\odot}$ , is derived *a posteriori* from observations. A reduction of iron stellar yields by a factor of about two has been inferred in recent researches (e.g., Wiersma et al. 2009; Yates et al. 2013). Power-law exponents within the range,  $-3 < -p < -2$ , produce results lying between the above mentioned extreme cases.

Semiempirical oxygen-to-iron yield ratios inferred for disk population are consistent with their counterparts inferred from star evolution theory,  $\hat{p}_{\text{Fe}}/\hat{p}_{\text{O}} \approx 0.15$ , restricted to SNII progenitors (Acharova et al. 2013), which is shown in Fig. 8 as a dotted horizontal line.

It is worth remembering semiempirical yield ratios plotted in Fig. 8 (full curves) are expressed in the light of simple MCBR chemical evolution models using the regression line of the empirical [Fe/H]-[O/H] relation, via Eq. (34), where the lowest iron abundances are supposed in absence of np processes i.e. from SNII progenitors. Under the alternative assumption of equal  $\phi_{\text{Fe}_{\text{sp}}}$ - $\phi_{\text{O}}$  relation for different subsamples, the lowest iron abundance related to sp processes should be reduced by a factor of about 0.4 at most, according to the results listed in Table 12.

On the other hand, theoretical yield ratios plotted in Fig. 8 (symbols) relate to SNII progenitors and, for this reason, have to be compared with the starting point (lowest iron abundance) of each curve. Taking into account the above mentioned uncertainties, an inspection of Fig. 8 shows agreement to an acceptable extent for subsolar iron abundance say, while the contribution from np processes (mainly related to SNIa progenitors) has to be considered for supersolar iron abundance (e.g., Wiersma et al. 2009).

If the iron-to-oxygen yield ratio increases with the metal abundance,  $Z$ , while the integrated stellar yield for massive stars decreases with  $Z$ , it may be interpreted as an increase of the np contribution with  $Z$ , which implies an increase of SNIa rate with  $Z$  compared to SNII.

In this view, passing from lower to larger iron abundances, semiempirical iron-to-oxygen yield ratios are increased by a factor of about 2 for HH subsample, 2.5 for ND and DD subsample, 5 for KD subsample. Then np processes appear to be more efficient during thick disk evolution than during thin disk and halo evolution, according to recent results implying a thick disk formation initially in starburst and then more quiescent, over a time scale of 4-5 Gyr (Haywood et al. 2031; Snaith et al. 2014).

A lower contribution to Fe abundance from np processes, by a factor 1.15, inferred *a posteriori* from observations in a recent research (Acharova et al. 2013) seems to be in contradiction with the empirical [Fe/H]-[O/H] relation, expressed by Eq. (4) or Eq. (5).

## 5 Conclusion

A linear [Fe/H]-[O/H] relation has been inferred from different populations sampled in a recent research (Ra13), namely HH (halo,  $N = 44$ ); KD (thick disk,  $N = 237$ ); ND (thin disk,  $N = 538$ ). Oxygen and iron empirical differential abundance distribution (EDAD) have been determined for different subsamples, together with related theoretical differential abundance distribution (TDAD), within the framework of simple multistage closed-(box+reservoir) (MCBR) chemical evolution models.

The evolution of iron vs. oxygen mass abundance has been deduced from the empirical [Fe/H]-[O/H] relation, and iron production via processes related to simple primary (sp) and non simple primary (np) elements (sp and np processes, respectively), has been estimated in two different alternatives. Iron TDAD, inferred from empirical [Fe/H]-[O/H] relation and oxygen EDAD, has been determined for different subsamples.

Iron-to-oxygen yield ratios have been deduced from the data in the framework of simple MCBR chemical evolution models, including an example of

comparison with theoretical counterparts computed for SNII progenitors with both subsolar and supersolar initial metallicity, under the assumption of power-law stellar initial mass function (IMF).

Oxygen and iron TDAD have been inferred from the data for different populations, in the opposite limit of inhomogeneous mixing due to cosmic scatter obeying a lognormal distribution whose mean and variance have been evaluated from the related subsample.

The main results, concerning (a) iron production via sp and np processes; (b) evolution and flow rate; (c) iron-to-oxygen yield ratios; are summarized as follows.

- (a1) Earlier results inferred from poorer subsamples (C13b) are supported in the sense that stars display along a “main sequence”, expressed as  $[\text{Fe}/\text{H}] = a[\text{O}/\text{H}] + b \mp \Delta b$ . For unit slopes,  $a = 1$ , a main sequence relates to constant  $[\text{O}/\text{Fe}]$  abundance ratio. The special cases,  $(a, b, \Delta b) = (3/2, -1/8, 3/8), (4/3, -2/15, 4/15)$ , imply only a few stars lie outside the main sequence within the errors.
- (a2) Regardless of the population, regression line slope estimators do not fit to the unit slope within  $\mp 3\hat{\sigma}_a$  and exhibit different values, which implies SNIa events contributed to a fraction of iron production to a different extent: lower for halo population and larger for thick disk population, with thin disk population lying between the above mentioned two.
- (a3) If lowest iron abundances in subsample stars arose from sp processes, then a comparable amount of iron was produced via sp and np processes with regard to F stage for disk population and after iron peak for halo population. The above result holds for thin disk population with regard to E stage, contrary to thick disk population, where iron production via np processes is dominant. A similar trend is shown by thin disk population, but not by halo population, under the alternative assumption of equal  $\phi_{\text{Fe}_{\text{sp}}}-\phi_{\text{O}}$  relation for different subsamples leaving its counterpart, related to thick disk population, unchanged.
- (a4) Iron TDAD, inferred from the empirical  $[\text{Fe}/\text{H}]-[\text{O}/\text{H}]$  relation and oxygen TDAD determined from linear fits, yields a satisfactory agreement with iron EDAD via a nearly linear trend for each stage.
- (a5) A cosmic scatter, obeying a lognormal distribution, due to homogeneous mixing in chemical evolution models, gives a TDAD which is not in agreement with the EDAD of the disk, and therefore this is not a valid alternative to explain it. However, this possibility remains still open for the halo.

- (b1)** Earlier results inferred from poorer subsamples (Caimmi and Milanese 2009; Caimmi 2012a) are supported in the sense that oxygen EDAD can be linearly fitted with regard to three different stages related to different abundance ranges, namely: assembling (A, low abundance); formation (F, middle abundance); evolution (E, high abundance). A similar trend is shown by iron EDAD. Within the framework of simple MCBR chemical evolution models (Caimmi 2011a; 2012a), each stage is characterized by a different inflow regime: A - strong inflow; F - (nearly) steady state inflow; E - weak inflow or outflow. A (nearly) steady state inflow regime is in agreement with results from hydrodynamical simulations (e.g., Finlator and Davé 2008; Davé et al. 2011a,b, 2012). The outflow rate related to thick and thin disk evolution is less than, but comparable to, outflow rate related to halo evolution, which is known to be high (e.g., Hartwick 1976). A low outflow rate related to disk evolution would imply (i) the halo subsample considered in the current research is representative of the inner halo, and (ii) a higher outflow rate relates to the outer halo.
- (b2)** Under the assumption that the gas left after the evolution of the thick disk was used for building up the thin disk, the two subsystems exhibit comparable masses according to recent investigations (Haywood et al. 2013; Snaith et al. 2014).
- (c1)** Within the framework of simple MCBR chemical evolution models (Caimmi 2011a; 2012a), iron-to-oxygen yield ratios, inferred from the empirical  $[\text{Fe}/\text{H}]-[\text{O}/\text{H}]$  relation for different subsamples, are consistent with theoretical results from SNII progenitor nucleosynthesis (Portinari et al. 1998; Wiersma et al. 2009), provided substantial iron production arises from SNIa events for supersolar abundances.

## References

- [1] Acharova, I.A., Gibson, B.K., Mishurov, Yu.N., Kovtyukh, V.V.: 2013, *Astron. Astrophys.*, 557, A107.
- [2] Bekki, K.: 2013, *Astrophys. J.*, 779, 9.
- [3] Caimmi, R.: 2007, *New Astron.*, 12, 289.
- [4] Caimmi, R.: 2011a, *Ser. Astron. J.*, 183, 37.
- [5] Caimmi, R.: 2011b, *New Astron.*, 16, 337.

- [6] Caimmi, R.: 2012a, *Ser. Astron. J.*, 185, 35.
- [7] Caimmi, R.: 2012b, Intellectual Archive, 1, 71, ISSN 1929-4700 Toronto. (arxiv 1111.2680).
- [8] Caimmi, R.: 2013a, *Ser. Astron. J.*, 186, 25. (C13a).
- [9] Caimmi, R.: 2013b, *Ser. Astron. J.*, 187, 19. (C13b).
- [10] Caimmi, R., Milanese, E.: 2009, *Astrophys. Space Sci.*, 323, 147.
- [11] Carollo, D., Beers, T.C., Lee, Y.S., et al.: 2007, *Nature*, 318, 1020.
- [12] Carollo, D., Beers, T.C., Chiba, M., et al.: 2010, *Astrophys. J.*, 712, 692.
- [13] Carretta, E., Gratton, R.G., Sneden, C.: 2000, *Astron. Astrophys.*, 356, 238.
- [14] Conroy, C., Dutton, A.A., Graves, G.J., Trevor Mendel, J., van Dokkum, P.G.: 2013, *Astrophys. J.*, 776, L26.
- [15] Davé, R., Finlator, K., Oppenheimer, B.D.: 2011a, *Mon. Not. R. Astron. Soc.*, 415, 11.
- [16] Davé, R., Finlator, K., Oppenheimer, B.D.: 2011b, *Mon. Not. R. Astron. Soc.*, 416, 1354.
- [17] Davé, R., Finlator, K., Oppenheimer, B.D.: 2012, *Mon. Not. R. Astron. Soc.*, 421, 98.
- [18] Doane, J.S., Mathews, W.G.: 1993, *Astrophys. J.*, 419, 573.
- [19] Finlator, K., Davé, R.: 2008, *Mon. Not. R. Astron. Soc.*, 385, 2181.
- [20] Gratton, R.G., Carretta, E., Matteucci, F., Sneden, C.: 2000, *Astron. Astrophys.*, 358, 671.
- [21] Hartwick, F.D.A.: 1976, *Astrophys. J.*, 209, 418.
- [22] Haywood, M.: 2001, *Mon. Not. R. Astron. Soc.*, 325, 1365.
- [23] Haywood, M., Di Matteo, P., Lehnert, M.D., Katz, D., Gómez, A.: 2013, *Astron. Astrophys.*, 560, A109.
- [24] Isobe, T., Feigelson, E.D., Akritas, M.G., Babu, G.J.: 1990, *Astrophys. J.*, 364, 104.

- [25] Israelian, G., Rebolo, R., Garcia-Lopez, R.J., Bonifacio, P., Molaro, P., Basri, G., Shchukina, N.: 2001, *Astrophys. J.*, 551, 833.
- [26] Lopez-Sanchez, A.R.: 2010, *Astron. Astrophys.*, 521, A63.
- [27] Malinie, G., Hartmann, D.H., Clayton, D.D., Mathews, G.J.: 1993, *Astrophys. J.*, 413, 633.
- [28] Pagel, B.E.J.: 1989, The G-dwarf Problem and Radio-active Cosmochronology. In: Beckman J.E., Pagel B.E.J. (eds.) *Evolutionary Phenomena in Galaxies*, p.201. Cambridge University Press, Cambridge.
- [29] Pagel, B. E. J., Tautvaisiene, G.: 1995, *Mon. Not. R. Astron. Soc.*, 276, 505.
- [30] Pagel, B.E.J., Patchett, B.E.: 1975, *Mon. Not. R. Astron. Soc.*, 172, 13.
- [31] Portinari, L., Chiosi, C., Bressan, A.: 1998, *Astron. Astrophys.*, 334, 505.
- [32] Ramírez, I., Allende Prieto, C., Lambert, D.L.: 2007, *Astron. Astrophys.*, 757, 164.
- [33] Ramírez, I., Meléndez, J., Chanamé, J.: 2012, *Astrophys. J.*, 757, 164.
- [34] Ramírez, I., Allende Prieto, C., Lambert, D.L.: 2013, *Astrophys. J.*, 764, 78. (Ra13).
- [35] Rieke, G.H., Loken, K., Rieke, M.J., Tamblyn, P.: 1993, *Astrophys. J.*, 412, 99.
- [36] Rocha-Pinto, H.J., Maciel, W.J.: 1996, *Mon. Not. R. Astron. Soc.*, 279, 447.
- [37] Ryan, S.G., Norris, J.E.: 1991, *Astron. J.*, 101, 1865.
- [38] Searle, L., 1972. Star Formation and the Chemical History of Galaxies. In: Cayrel de Strobel, G., Delplace, A.M. (eds.) *L'Agés des Etoiles*, Observatoire de Paris-Meudon, p. 52.
- [39] Searle, L., Sargent, W.L.W.: 1972, *Astrophys. J.*, 173, 25.
- [40] Snaith, O.N., Haywood, M., Di Matteo, P., Lehnert, M.D.: 2014, *Astrophys. J.*, 781, L31.

- [41] Takada-Hidai, M., Takeda, Y., Sato, S., Sargent, W.L., Lu, L., Barlow, T., Jugeku, J.: 2001, *New Astron. Rev.*, 45, 549.
- [42] Wiersma, R.P.C., Schaye, J., Theuns, T., Dalla Vecchia, C., Tornatore, L.: 2009, *Mon. Not. R. Astron. Soc.*, 399, 574.
- [43] Wilmes, M., Köppen, J.: 1995, *Astron. Astrophys.*, 294, 47.
- [44] Woosley, S. E., Weaver, T. A., 1995. *Astrophys. J. Supp.* 101, 181.
- [45] Yates, R.M., Henriques, B., Thomas, P.A., Kauffmann, G., Johansson, J., White, S.D.M.: 2013, *Mon. Not. R. Astron. Soc.*, 435, 3500.

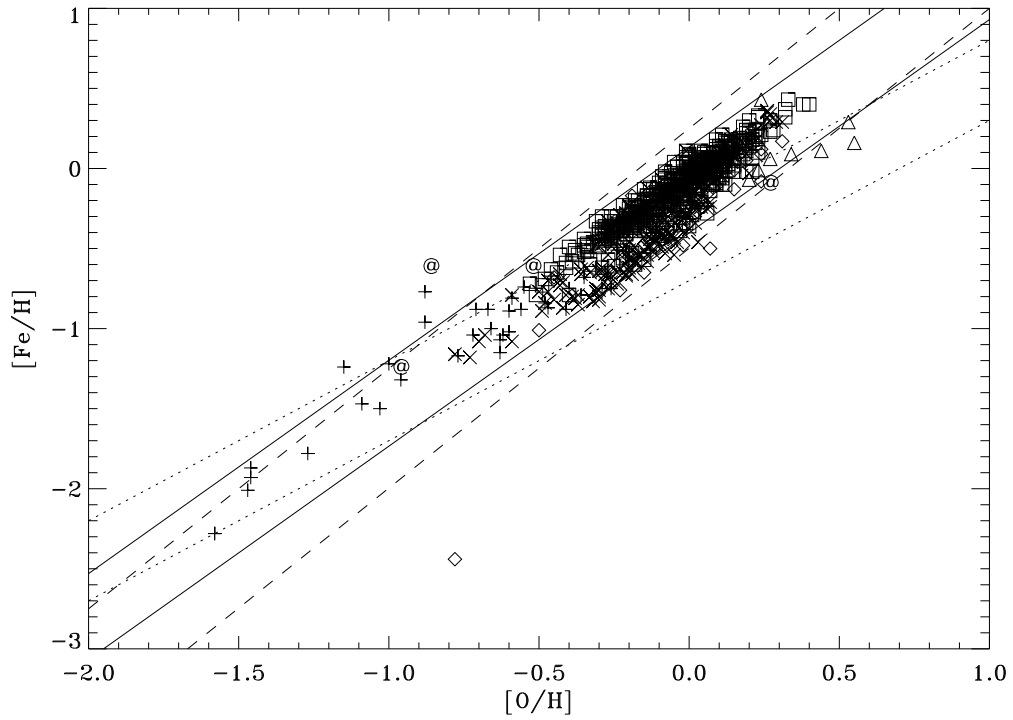


Figure 1: The empirical  $[\text{Fe}/\text{H}]$ - $[\text{O}/\text{H}]$  relation for HD stars sampled in Ra13. Caption of symbols: normal main sequence dwarf stars - squares (NDn), saltires (KDn), diagonalized squares (KNn), crosses (HHn); cool main sequence dwarf stars - triangles (HDc); giants - diamonds (HDg); outliers - “at” symbols (HDo). Also shown for comparison are the “main sequences”,  $[\text{Fe}/\text{H}] = [\text{O}/\text{H}] - 0.45 \pm 0.25$  (dotted),  $2[\text{Fe}/\text{H}] = 3[\text{O}/\text{H}] - 0.25 \pm 0.75$  (dashed),  $3[\text{Fe}/\text{H}] = 4[\text{O}/\text{H}] - 0.40 \pm 0.80$  (full). Typical error bars are of the order of the symbol dimensions. See text for further details.

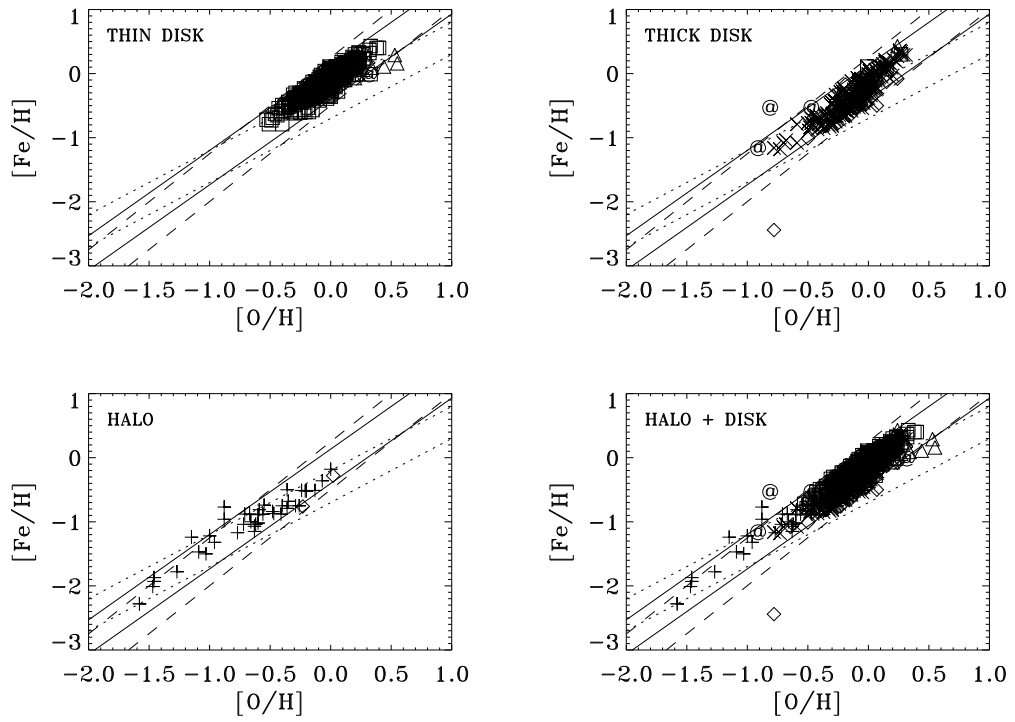


Figure 2: The empirical  $[\text{Fe}/\text{H}]-[\text{O}/\text{H}]$  relation for ND (top left), KD (top right), HH (bottom left), HD (bottom right) stars sampled in Ra13. Bottom right panel is the repetition of Fig. 1 for better comparison. Other captions as in Fig. 1.

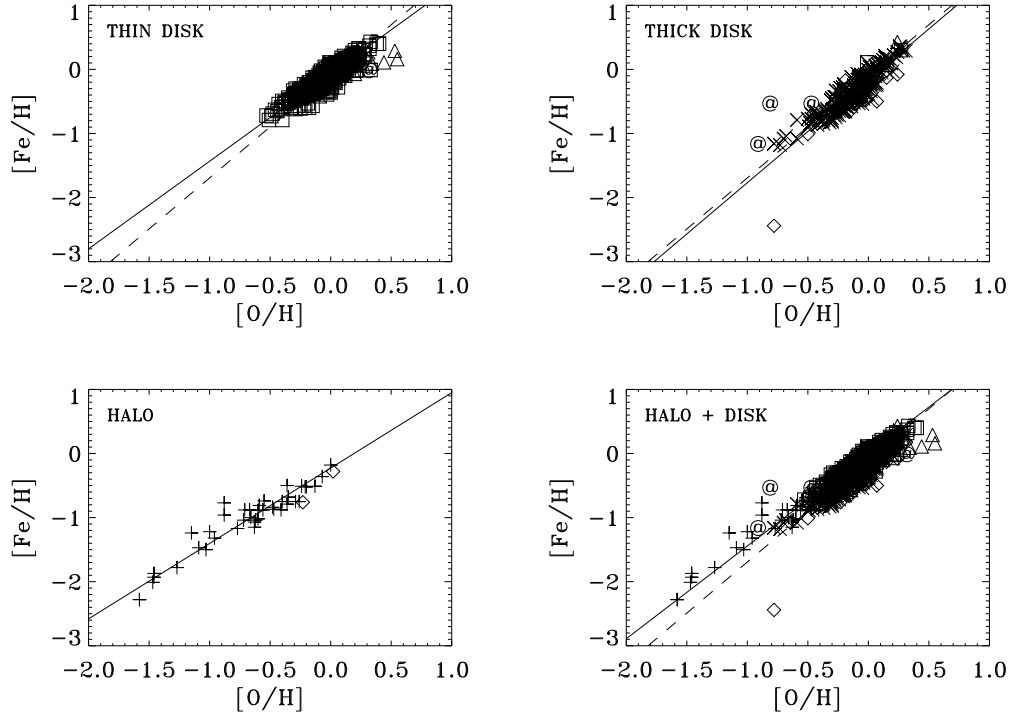


Figure 3: Regression lines,  $[\text{Fe}/\text{H}] = a[\text{O}/\text{H}] + b$ , inferred for different populations, ND (top left), KD (top right), HH (bottom left), HD (bottom right). Dashed lines relate to  $\text{DD} = \text{ND} + \text{KD} + \text{KN}$ . Slope and intercept values are taken from related estimators listed in Table 3. The caption of the symbols is the same as in Fig. 1.

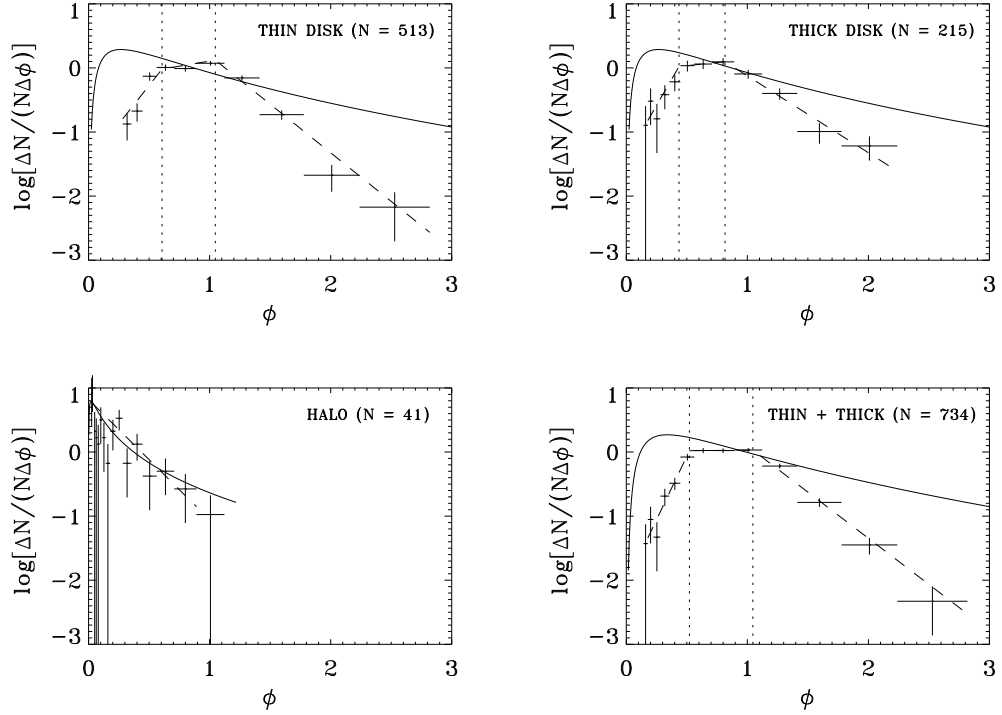


Figure 4: Oxygen empirical differential abundance distribution (EDAD) inferred from ND, KD, DD = ND + KD + KN, HH, subsamples (from top left in clockwise sense). Lower uncertainties attaining the horizontal axis (decreasing up to negative infinity) relate to bins populated by a single star. Dashed straight lines represent regression lines to points defining bins populated by at least two stars. Transition points between adjacent stages are marked as dotted vertical lines. Full curves represent oxygen theoretical differential abundance distribution (TDAD) due to intrinsic scatter obeying a lognormal distribution with mean and variance inferred from the data. See text for further details.

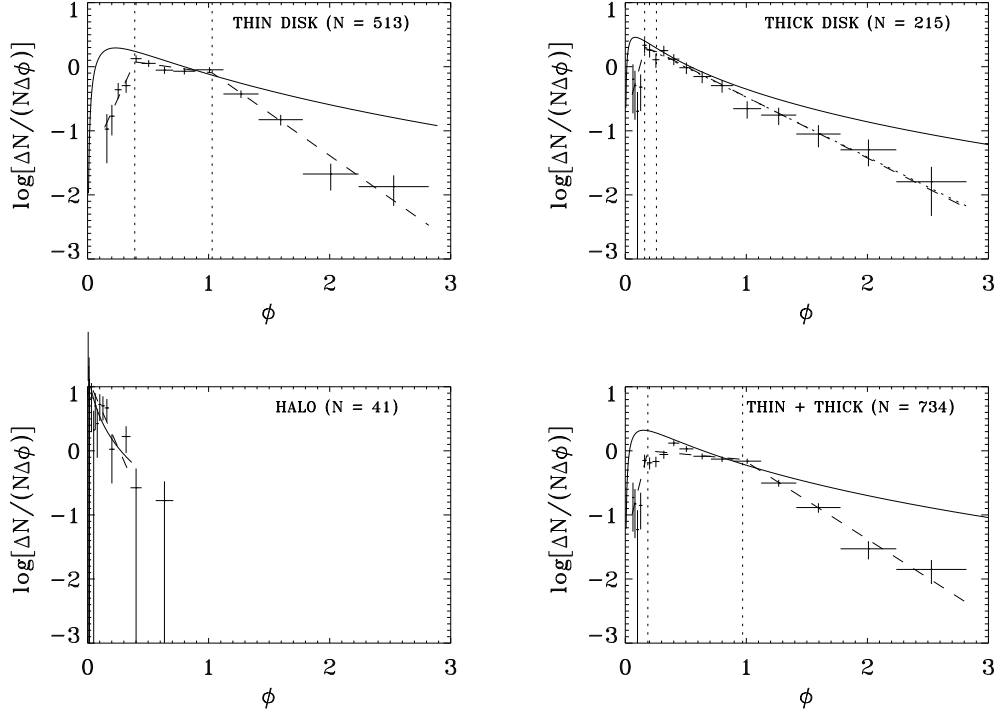


Figure 5: Iron empirical differential abundance distribution (EDAD) inferred from ND, KD, DD = ND + KD + KN, HH subsamples (from top left in clockwise sense). Lower uncertainties attaining the horizontal axis (decreasing up to negative infinity) relate to bins populated by a single star. Dashed straight lines represent regression lines to points defining bins populated by at least two stars. The dotted straight line on top right panel represents the regression line for the whole declining part of the EDAD. Transition points between adjacent stages are marked as dotted vertical lines. Full curves represent iron theoretical differential abundance distribution (TDAD) due to intrinsic scatter obeying a lognormal distribution with mean and variance inferred from the data. See text for further details.

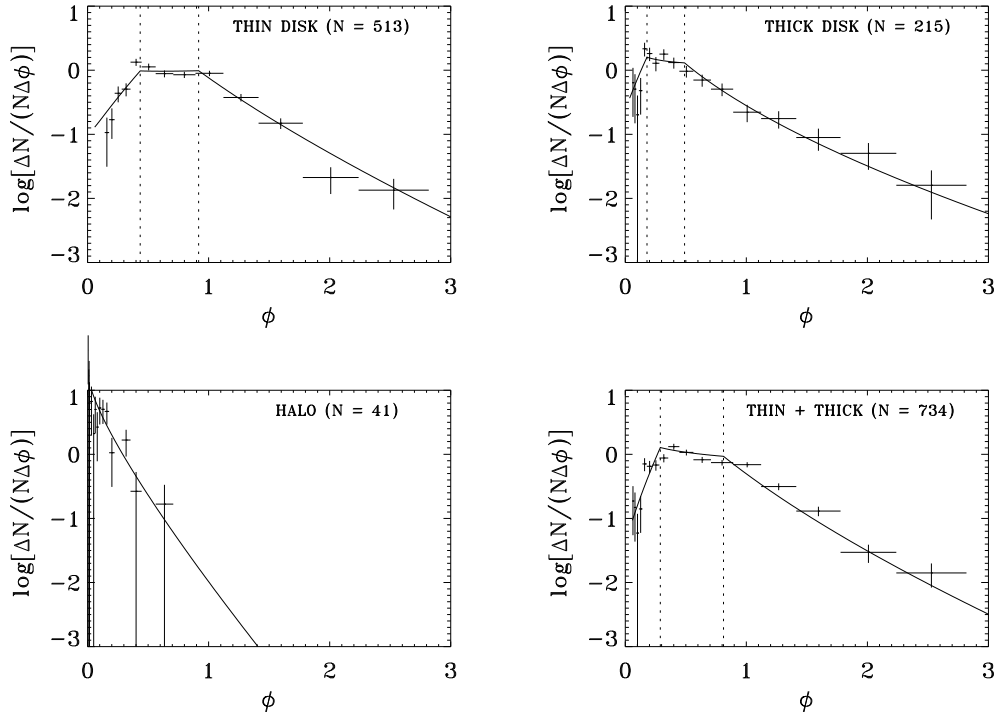


Figure 6: Iron theoretical differential abundance distribution (TDAD) inferred from the empirical  $[\text{Fe}/\text{H}]-[\text{O}/\text{H}]$  relation and oxygen empirical differential abundance distribution (EDAD), with regard to ND, KD, DD, HH subsamples (from top left in clockwise sense). Iron EDAD is also shown for comparison (captions as in Fig. 5). Dotted vertical lines mark steady state (SS) inflow regime inferred from oxygen EDAD. See text for further details.

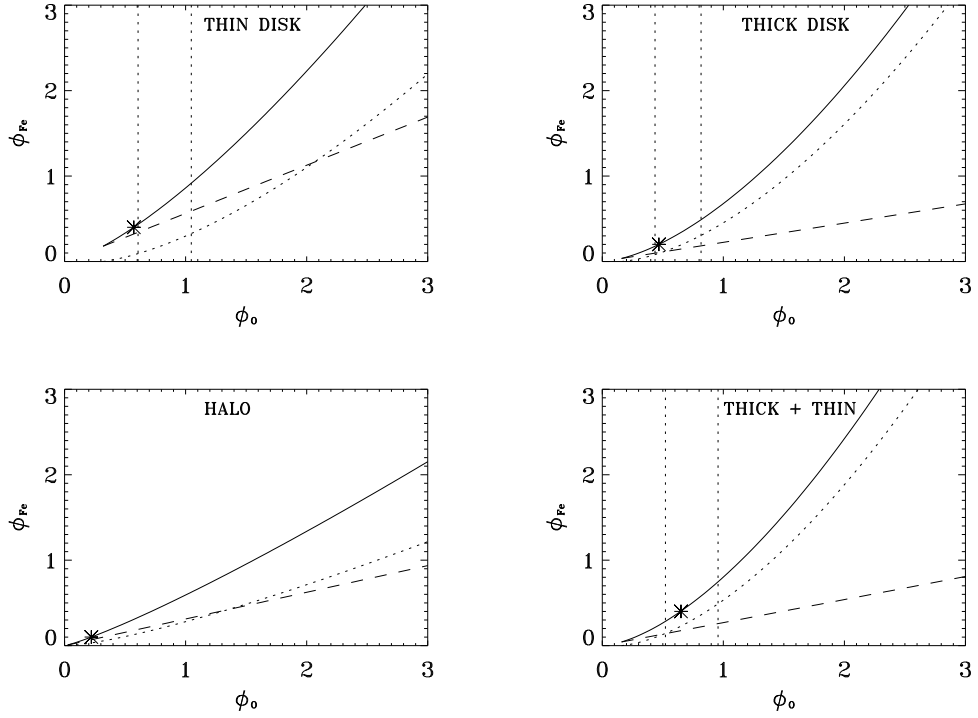


Figure 7: Iron vs. oxygen mass abundance (normalized to solar values), inferred from the empirical  $[\text{Fe}/\text{H}]-[\text{O}/\text{H}]$  relation, related to ND, KD, DD = KD + ND + KN, HH subsamples (from top left in clockwise sense), under the assumption of initial abundance fraction,  $(\phi_{\text{Fe,sp}}/\phi_{\text{Fe}})_{\text{m}} = 1$ . Dashed, dotted and full curves relate to iron production via sp, np, sp+np processes, respectively. Dotted vertical lines mark the abundance range related to the steady state (SS) inflow regime inferred from oxygen empirical differential abundance distribution (EDAD). The abundance peak exhibited by iron EDAD is denoted by an asterisk on related full curve. See text for further details.

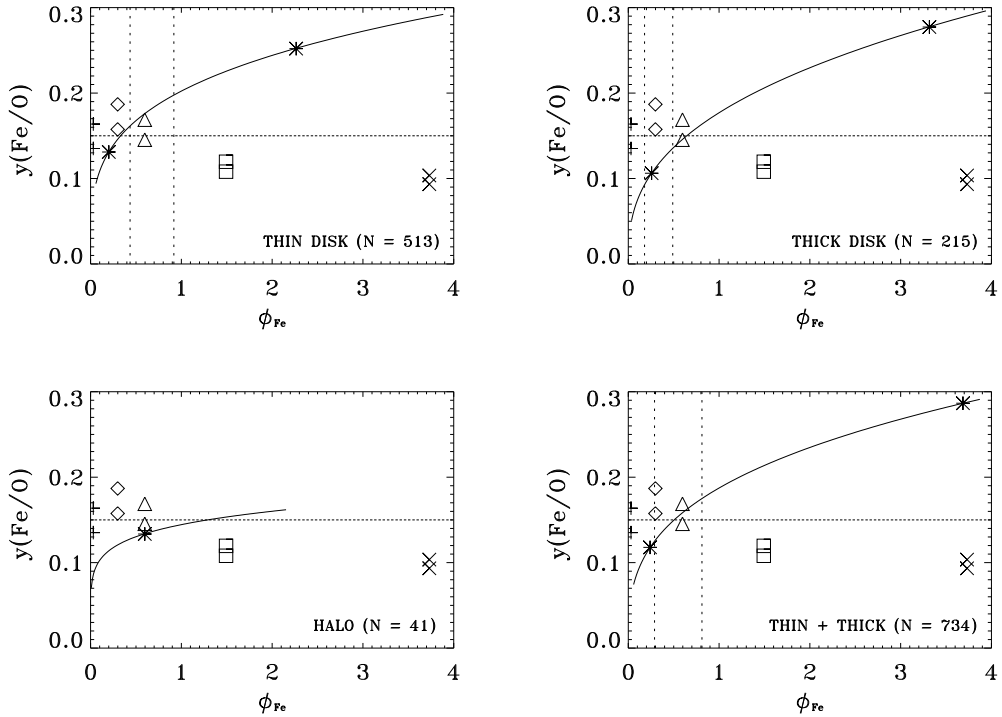


Figure 8: The yield ratio,  $y(\text{Fe}/\text{O}) = \hat{p}_{\text{Fe}}/\hat{p}_{\text{O}}$ , expressed by Eq. (34), as a function of iron abundance,  $\phi_{\text{Fe}}$ , for ND, KD, DD, HH subsample (from top left in clockwise sense). Dotted vertical lines mark different stages inferred from oxygen EDAD. Asterisks on each curve represent yield ratios inferred from EDAD regression lines for both A stage (left, with the exclusion of HH subsample) and E stage (right), regardless of iron abundance. Theoretical yield ratios for a power-law stellar initial mass function (IMF) with exponent,  $-p = -2$  (down) and  $-p = -3$  (up), restricted to  $9 \leq m/m_{\odot} \leq 20$ , are shown for different initial metal abundance,  $Z = 0.0004$  (crosses),  $0.004$  (diamonds),  $0.008$  (triangles),  $0.02$  (squares),  $0.05$  (saltires), where  $Z_{\text{Fe}}/Z = (Z_{\text{Fe}})_{\odot}/Z_{\odot}$  is assumed. Power-law exponents within the range,  $-3 < -p < -2$ , produce results lying between the above mentioned extreme cases. Different mass ranges imply theoretical yield ratios reduced by a factor up to about two. A semiempirical yield ratio inferred for disk population, restricted to SNII progenitors, is shown as a dotted horizontal line. See text for further details.